Monitoring snow using geostationary satellite retrievals
during the SAAWSO project

Robert M Rabin[1]
NOAA/National Severe Storms Laboratory
Norman OK USA 73072
and
NOAA/Cooperative Institute for Meteorological Satellite Studies
University of Wisconsin-Madison USA 53706

Ismail Gultepe
Environment Canada, Cloud Physics and Severe Weather Research Section
Toronto, ON M3H5T4

Robert J. Kuligowski
Center for Satellite Applications and Research, NOAA/National Environmental Satellite, data, and Information Service (NESDIS), College Park, MD

Andrew K. Heidinger
NOAA/NESDIS/STAR/Advanced Satellite Products Branch, Madison, Wisconsin

---

[1]

Dr.Robert Rabin, 120 David L. Boren Blvd, Norman OK 73072 USA, bob.rabin@noaa.gov

Abstract

The SAAWSO (Satellite Applications for Arctic Weather and SAR (Search And Rescue) Operations) field programs were conducted by Environment Canada near St Johns, NL and Goose Bay, NL in the winters of 2012-13 and 2013-14, respectively. The goals of these programs were to validate satellite-based nowcasting products, including snow amount, wind intensity, and cloud physical parameters (e.g., cloud cover), over northern latitudes with potential applications to Search And Rescue (SAR) operations. Ground based in-situ sensors and remote sensing platforms were used to measure microphysical properties of precipitation, clouds and fog, radiation, temperature, moisture and wind profiles. Multi-spectral infrared observations obtained from Geostationary Operational Environmental Satellite (GOES)-13 provided estimates of cloud top temperature and height, phase (water, ice), hydrometer size, extinction, optical depth, and horizontal wind patterns at 15-minute intervals. In this work, a technique developed for identifying clouds capable of producing high snowfall rates and incorporating wind information from the satellite observations is described. The cloud top physical properties retrieved from operational satellite observations are validated using measurements obtained from the ground-based in-situ and remote sensing platforms collected during two precipitation events: a blizzard-heavy snow storm case and a moderate snow event. The retrieved snow precipitation rate are found to be comparable to these of ground based platform measurements in the heavy snow event.

1. Introduction

The remote detection of precipitation is most reliably accomplished with active sensors such as weather radar. Information on precipitation intensity andhydrometeor type can be inferred from the reflectivity and polarization parameters observed by radar. For S-band radars, it is possible to obtain a 3-D mapping of precipitation within clouds to distances of roughly 200 km. However, due to earth curvature and beam broadening, it is not possible to obtain radar measurements at the surface. The measurements from the lowest radar elevation scans are a few km above the surface at the longer ranges. Detection of sub-precipitation size particles, such as ice crystals, drizzle, fog, etc., requires the use of shorter wavelength radar such as x-band and cloud radars. In the case of very small particles (aerosols for example) lidar is required. The maximum range of x-band radars and lidars is about 50 km and 10 km respectively. In all cases, precipitation rate cannot be directly measured by radar. Rather, precipitation rate must be inferred from bulk relationships of reflectivity with precipitation rate.   These relationships are most uncertain for frozen precipitation types. Hence, estimation of snowfall rates (and snow water equivalent) is subject to large errors as compared to rain rates (RASMUSSEN ET AL., 2003). In addition, ambiguity in determining precipitation phase exists with measurements of radar reflectivity alone. Dual polarimeteric observations, such as those now available from the WSR-88D radar network in the U.S., can be used to distinguish among rain, snow, hail, etc.

Given the limited coverage of individual active sensors, however, widespread coverage of ground-based radar and lidar is not practical in most remote regions of Canada. A space-borne

dual-frequency radar launched in 2014 (NASA Global Precipitation Mission program) offers a potential for widespread measurements of radar reflectivity along the satellite orbital paths (HOU ET AL., 2014). However, the frequency of observations is less than hourly and hence must be supplemented with passive (radiometric) measurements from other satellites to provide more continuous temporal coverage. Techniques for precipitation estimation have been developed using microwave and infrared emissions over the past three decades.

Microwave radiation emanates from the interior of cloud layers (in addition to the surface), while infrared radiation is predominately from the cloud tops. Hence, passive microwave measurements contain information on the vertically integrated ice and water content of clouds, which is used in the retrieval of precipitation. Radiation emitted from the surface can interfere with the signal from clouds. Since the microwave emission is relatively small over water, retrieval of precipitation is more reliable over oceans than from over land surfaces. Until recently, retrieval techniques have been developed for rain rather than snowfall (OLSON ET AL., 1996). The horizontal resolution of the passive microwave measurements from polar orbiting satellites is approximately 15-40 km. The use of infrared observations to deduce cloud characteristics and monitor precipitation has the advantage of more frequent sampling from geostationary satellites. The horizontal resolution of these observations is approximately 5-10 km at latitudes of 45-60 degrees. Limitations of geostationary satellites due to viewing angle and resolution are an issue poleward of about 60 degrees.

The goal of this work is to summarize a technique for snow precipitation estimation based on estimates of cloud top properties derived from multi-spectral infrared observations obtained from Geostationary Operational Environmental Satellite (GOES)-13 and validate the results using in-situ observations. A heavy snow storm near St John's NL on 10-11 January 2013

and a moderate snow event near Goose Bay NL on 6 April 2014 were used in the analysis. The potential for monitoring snowfall at the surface from estimates of cloud top temperature and height, phase (water, ice), hydrometer size, optical depth, inferred altitude of the dendritic ice growth zone, horizontal wind patterns near cloud tops, and a GOES precipitation algorithm are evaluated. The time evolution of these satellite estimates are validated using measurements obtained from ground-based in-situ and remote sensing platforms during the both precipitation events.

2. Observations and GOES Data

Observations collected for satellite applications of Arctic weather and SAR (Search and Rescue) operations (SAAWSO) project during the winters of 2012-13 and 2013-14 over St. John's and Goose Bay, NL, Canada, are used in this work. Details of the observations can be found in GULTEPE ET AL (2014; 2015). During SAAWSO project, ground base observations of fog, drizzle, snow, and wind and turbulence together with conventional measurements of meteorological parameters and remote sensing based parameters (e.g., radar precipitation reflectivity, lidar backscattering, and Profiling MicroWave Radiometer (PMWR) Liquid water content (LWC), relative humidity (RH), and temperature (T) products) were collected to better understand fog and cloud, and precipitation occurrence and its prediction for nowcasting applications.

During this project, imager scans from GOES-13 were routinely available at 15-minute intervals. The field sites of St Johns and Goose Bay are near to the eastern edge of the image domains at 02 and 32 minutes after each hour and thus were not used, but satellite sectors scanned at 15 and 45 minutes after each hour are sufficiently large to include better coverage for use in this study. The GOES-13 Imager data contains one shortwave (SW) visible and 4 infrared

(IR) bands with roughly 2- and 6-km resolution respectively over the field sites. Retrievals of cloud top properties from these data were obtained in real-time from the Cooperative Institute for Meteorological Satellite Studies (CIMSS) at the University of Wisconsin-Madison. These include estimates of cloud optical depth and effective particle diameter from the Daytime Cloud Optical and Microphysical Properties Algorithm (DCOMP, WALTHER AND HEIDINGER, 2012) and cloud top pressure, temperature and emissivity during both day and night. These retrievals form the basis of algorithms to be implemented on the next generation of geostationary satellites (GOES-R). The GOES-R satellites will contain additional spectral channels, horizontal resolution, and sampling frequency. The retrievals have been evaluated against aircraft measurements (ROEBELING ET AL, 2014).

3. Method

i)Precipitation estimates from infrared satellite imagery

Techniques for estimating precipitation from the GOES based infrared observations utilize statistical relations between cloud top temperature and observed rain rate at the surface. The techniques generally perform best for convective precipitation which have well defined cold cloud tops (SCOFIELD AND KULIGOWSKI, 2003). However, the aerial coverage of precipitation tends to be overestimated when widespread anvils are present. Satellite-based estimates of rainfall have been used operationally by the National Oceanographic and Atmospheric Administration (NOAA) since the late 1970's (SCOFIELD 1987, VICENTE ET AL. 1998). The Hydro-Estimator (H-E; SCOFIELD 1987 AND KULIGOWSKI 2003) has been the operational algorithm since 2002. The Self-Calibrating Multivariate Precipitation Retrieval (SCaMPR) algorithm combines the relative strengths of infrared-based and microwave-based estimates of precipitation (KULIGOWSKI ET AL. 2014). SCaMPR is being refined and evaluated for future use

with the GOES-R satellite. It appears to detect both stratiform and convective precipitation patterns. In this work, the SCaMPR method is modified to be used for cold climate snow estimates and then it is applied for SAAWSO project conditions. The performance of this method is explored in this paper.

ii)Dendritic Ice zone

Estimates of Cloud Top Pressure (CTP), Cloud Top Temperature (CTT), and Effective Cloud Amount (ECA) from the GOES-13 Imager will be used to infer temperature below cloud top where saturated ascent occurs through a deep layer. The purpose is to estimate locations of high precipitation efficiency where dendritic ice crystal growth is taking place. Studies have identified a relatively narrow temperature range (centered near -15 ºC) at which dendritic ice crystal growth by deposition and efficient snow production occurs (e.g., AUER AND WHITE, 1982). Typically, this occurs near the 600 hPa level during heavy snow storms in the eastern U.S. An operational technique has been proposed which evaluates areas where strong forcing for ascent coincides with regions of sufficient moisture and temperatures favorable for maximum depositional growth (WETZEL AND MARTIN, 2002). The analysis technique outlined here, together with analyzes from numerical models may be of use in assessment of such regions.

The ECA is used to screen out thin or broken cloud layers. A minimum threshold of 98% is used to process cloud information. Next the CTP and CTT are used to compute the equivalent potential temperature (EPT) at cloudy points. For points where CTP is less than 600 hPa, the pressure at which in-cloud temperatures are near -15ºC, P(-15ºC), is computed from the EPT. This assumes a nearly moist adiabatic lapse rate from cloud top to the pressure level where the temperature is -15ºC. The derived P(-15ºC) can be useful to indicate the pressure level where

dendritic growth may be important (if upward air motion is present). Comparisons of the estimated pressure levels from this technique with those observed from rawinsonde profiles suggest an uncertainty of about 50 hPa (RABIN AND HANNA, 2008). Extension of the technique to estimate temperature profiles in the lower layers (much below 600 hPa) becomes more uncertain because of deviations from the moist adiabatic lapse rate, such as inversions which are often observed closer to the surface. Output from satellite-based QPE algorithms (described below) is used to identify areas where deep ascent is likely occurring and the technique can be applied. The GOES Hydroestimator and SCaMPR QPE algorithms (courtesy of Robert J. Kuligowski, NOAA/NESDIS) are used for this purpose. An additional refinement is to utilize an analysis of upper-level divergence from satellite winds and mesoscale forecast model output to estimate the magnitude of upward motion in these regions.

iv)Atmospheric Motion Vectors from geostationary satellite

Satellite-based winds can be used to capture features on a more detailed scale than from conventional meteorological observations. Winds are estimated by tracking the displacement of cloud or water vapor features between consecutive images. Visible or infrared imagery can be used for this purpose (VELDEN ET AL., 2005). Use of infrared imagery from the water vapor absorption band (near 6.7 microns) has the advantage of tracking both clouds and moisture features, assumed to be moving with the wind. The radiation received at the satellite at this wavelength emanates from the upper troposphere. Hence, the derived winds are from layers roughly 200 hPa thick centered between about 500 to 100 hPa, depending on relative humidity in the upper troposphere. Examples of upper-level wind fields deduced from water-vapor imagery include jet maxima and divergent regions where vertical air motion and precipitation may be

forming or be enhanced (RABIN ET AL., 2004). An automated method for calculating water vapor winds, developed at CIMSS (VELDEN ET AL., 1997), was applied in real-time using the GOES-13 data. This includes kinematic parameters such as horizontal divergence near the 300 hPa level. These terms are computed after interpolating winds to constant pressure surfaces using a recursive filter (HAYDEN AND PURSER. 1995). Forecast wind fields from the U.S. Global Forecast System (GFS) numerical weather model are used as a first guess in the process of tracking features to estimate winds. The editing of wind vectors is kept at a minimum in order to include significant deviations from the model guess field. This allows the detection of perturbed flow aloft due to convection and other small-scale features that are not correctly captured by forecast models. A new set of winds is computed every 30 minutes from GOES-13 imagery.

v)Forecast model vertical air motion

Output from the Rapid Refresh Atmospheric Prediction (RAP) numerical weather model is used as an independent estimate of profiles of vertical air motion. The RAP is run by NOAA's National Centers for Environmental Prediction (NCEP). The version available for the locations in this study has a 13-km horizontal resolution. RAP forecasts are generated every hour. For purposes of this study, the forecast analysis is used which include commercial aircraft weather data, balloon data, radar data, surface observations, and satellite data.

4. Results

i)Blizzard-heavy snow event

A major winter storm affected the southeastern part of Newfoundland on 10-11 January 2013. High winds and heavy snow had severe impacts on St John's including widespread power

outages in the area. Snowfall totaled 48 cm at the St John's airport. A deepening upper level trough over southern Quebec at 00 UTC 10 Jan 13 moved east and developed into a cutoff low to the south of Newfoundland in the subsequent 24 hours. At the surface, a deepening surface low moved northeastward just to the south of Newfoundland by 00 UTC 11 January 13. A strong pressure gradient north of the track of the low was associated with high winds from the northeast during the passage of the storm. Wind gusts over 100 km hr^{-1} were recorded at the St John's airport.

A sequence of GOES-13 infrared satellite imagery with divergence at 300 hPa computed from satellite wind estimate is shown in Fig. 1. The upper level circulation is apparent in the cold top clouds (light gray) to the southwest of Newfoundland at 06 UTC 10 January 13. An extensive cloud band develops ahead of the circulation in the subsequent 6 hrs. Typical of synoptic-scale cyclones, the cloud feature exhibits a "comma" like structure by 12 UTC 10 January 13. The "head" or back end of the comma remains in the vicinity of southern Newfoundland for the remaining sequence of images (through 00 UTC, 12 January 2013). Strong upper-level divergence (greater than $40 \times 10 s^{-1}$) develops along the cloud band feeding into the comma. This is usually associated with upward air motion through a deep layer of the troposphere.

Images of the cloud top properties above the developing storm at 1815 UTC 10 January 2013 are shown in Fig. 2. In general, the cyclonic cloud feature approaching Newfoundland is associated with cloud top pressures and temperatures below 300 hPa (Fig. 2b) and -40ºC (Fig. 2a), respectively. The locations of largest hydrometeor sizes (Fig. 2c) are within the cold cloud shield, but not well correlated with the coldest temperatures. The largest optical depths (Fig. 2d)

appear to be skewed to the western edge of the cloud band. The entire region of this cloud shield is identified as ice from the cloud type algorithm (not shown).

The pressure level where the temperature is -15ºC shown as P(-15), diagnosed from cloud top temperature and pressure at 1815 UTC, is given in Fig. 3a. Typical of snow storms studied in the eastern U.S., the P(-15) is close to 600 hPa in southeast Newfoundland (+/- 50 hPa). The vertical air motion at 600 hPa, deduced from the RAP model analysis at 18 UTC is compared to the 300 hPa divergence in Fig. 3b. Suggestive of a deep layer of rising air motion, a broad region of upper level divergence (more than 30×10^{-5} s^{-s}) encompasses most of the cloud band. According to the RAP analysis, most of that region contains ascending air at 600 hPa (less than -5 $\mu b\ s^{-1}$). Fig. 3c only shows computed values of P(-15) where ascending air at 600 hPa is located. Comparing Fig. 3a and 3c, there are a few areas where relatively weak ascent or descent are located and the estimation of P(-15) may not be meaningful. The precipitation rate estimated from the SCaMPR algorithm is given in Fig. 3d. The precipitation is roughly collocated with the coldest cloud top temperatures. It also has similar coverage as the region of ascending air at 600 hPa. This suggests that locations of precipitation from SCaMPR could be used as a proxy of deep layer rising air motion (independent from model analysis). Locations of precipitation from SCaMPR and or upper-level divergence derived from satellite winds could be applied to estimated P(-15) to identify regions with potential for dendritic ice growth and heavy snow fall.

Surface observations of precipitation rate measured by a pluviometer are displayed in Fig. 4. Water equivalent snowfall was sampled at 1-minute intervals. Snowfall began at 1900 UTC on 10 January. Measurements stopped at 1012 UTC on 11 January due to a power outage caused by the storm. Heaviest rates occurred between 00-01 UTC on 11 January, although rates of 2-4 mm hr^{-1} were common from 20 UTC 10 January – 08 UTC 11 January.

Precipitable water measured from the Radiometrics PMWR showed a steady increase leading up to the time of precipitation onset (Fig. 5). Values more than doubled between 00 and 19 UTC on 10 January. Subsequent change was small with a slight decreasing trend until the power outage at 1012 UTC.

Integrated cloud liquid water path (LWP) (Fig. 5) measured also from the PMWR begins to exhibit significant short-term fluctuations after about 07 UTC on day1. An increase in the peak values began at 14 UTC with a few values of 0.1 measured after 16 UTC. A significant increase in the range of values occurred at 19 UTC, which corresponds to the time of the onset of precipitation. A decrease occurred later in the period, most notably after 08 UTC January 11.

The horizontal divergence at 300 hPa estimated from GOES wind data first became positive between 08-12 UTC 10 January (Fig. 6). With exception of the period between 13-16 UTC, the trend of the upper-level divergence was similar to that of the precipitable water. The peak occurred around 20-21 UTC 10 January, with a slight decrease subsequent to that time.

The following time series of cloud top parameters are based on average values with a box approximately 50x50km centered on the location of St John's. A spatial average was used to smooth out small-scale variability and possible mis-location of satellite pixels due to parallax effects. The estimated cloud top temperature, pressure, and inferred P(-15) are given in Figs. 6 and 7.

The passage of a cloud band prior to the onset of precipitation is evident in Fig. 6. Cloud top temperatures were colder than -45ºC with this feature between 07-11 UTC on day 1. Similar temperatures were measured from clouds overhead near the time of precipitation onset (18-19 UTC) on day 1. However, slightly warmer cloud tops were present during the period with the

heaviest precipitation, 00-01 UTC January 11 (-42ºC). This observation is consistent with the typical pattern of heaviest snowfall located to the south of the coldest cloud tops and tightest infrared temperature gradient (for example, STEIGERWALDT, 1986; KADIN, 1982). The cloud top temperature over St John's increased by 15ºC between 10-17 UTC January 11and remained above -30 ºC for the rest of the day. The time trends of cloud top pressure (Fig. 7) match those of temperature (Fig. 6). Minimum cloud top pressure was about 330 hPa when temperatures were coldest, with values of about 380 hPa during the period of heaviest snowfall. The cloud top pressure was greater than 520 hPa after 10 UTC January 11. The inferred values of P(-15) vary by about 100 hPa during the entire 2-day period. P(-15) is very close to 600 hPa at the onset time of precipitation, close to the pressure level typical of other major snow events. The values decreased to about 570 hPa by 07 UTC January 11, before increasing after that time. This implies the following temperature changes at the 600 hPa level: 1) 2-3 ºC warming from 19 UTC day 1 through 07 UTC January 11, and 2) 2-3 ºC cooling during the 07-23 UTC January 11 time period. These trends are similar to those observed in the temperature retrievals from the PMWRr (not shown).

Precipitation estimates from the satellite-based SCaMPR algorithm can be compared to the pluviometer observations in Fig. 4. Note that relatively low precipitation rates (up to 1 mm hr^{-1}) were erroneously inferred from the cold cloud band which passed overhead between 07-11 UTC on day 1. In addition, the onset of precipitation at 16 UTC was about 3 hours earlier than observed with the surface guage. However, the period of heaviest precipitation detected by SCaMPR (3-4 mm hr^{-1}) matches that observed by the pluviometer (Fig. 4).

The estimated cloud top effective particle diameter and optical depth obtained using GOES based retrieval technique are shown in Fig. 8. Since these retrieved quantities depend on

reflected solar radiation observed near in the GOES imager band 2 near 4 µm wavelength, they are only available during daylight hours when the solar elevation angle exceeds approximately 15 degrees. A doubling of estimated cloud top particle diameter from 15 to 30 µm occurred in the 7 hours prior to precipitation (12-19 UTC on day 1). In the mean, there appeared to also be significant increase in optical depth during this period. However, there is considerable scatter between points which raises uncertainty in the measurements.

A sequence of upper air soundings from the Mt Pearl site near St Johns are given in Fig. 9. In these, "Stuve" diagrams, lines of constant temperature and dew point are parallel to the y-axis; pressure or height is parallel to the x-axis. The thick curves are plots of temperature (right) and dew point (left) versus pressure. Clouds or saturation occur where the temperature and dew point are nearly equal.

The first sounding shown is from 10 January, 12 UTC, approximately 9 hours before the onset of precipitation. At that time, the sounding indicated a layer of near saturation between 550 and 250 hPa. However, a dry layer existed from 900 to 550 hPa. The mean cloud top temperature and pressure from the GOES retrievals within the 50x50 km box surrounding St Johns is plotted (CTOP). The horizontal and vertical red lines surrounding CTOP indicate the RMS of the cloud top pressure and temperature from the sample points within the box surrounding St Johns. The pressure level where dendritic ice growth is possible, from the satellite inferred P(-15), is labeled "Sat DGZ". In this case, there is no Dendritic Growth layer (DGZ), since a saturated layer did not exist in vicinity of the -15ºC layer.

The next available sounding was 12 hours later (00 UTC 11 January) at approximately the time of heaviest snowfall. In contrast to the previous sounding, it indicated the existence of a deep saturated layer from about 350 hPa to near the surface. From this sounding, a DGZ layer is

indicated where the air is saturated between -10 and -20 ºC. The P(-15) approximates the pressure of the middle of the DGZ, but is about 50 hPa too high.

The next available sounding was 24 hours later at 00 UTC 12 January after dissipation of the precipitation. At this time, the saturated layer was limited to 700 hPa to the surface, where the temperature was warmer than -10ºC. Hence, a DGZ was not present. There was a large variability (RMS) in the estimated mean pressure and temperature of CTOP, 500 hPa and -30ºC, respectively. This would indicate a scattered or broken cloud deck above the saturated layer previously mentioned.

It is difficult to accurately validate the CTOP values from the rawinsondes alone. Available measurements from the vertically pointed X-band radar near St Johns are used for validation of thick cloud conditions.

Figures 10 and 11 show the time variation of radar reflectivity and hydrometeor fall speeds versus height from the X-band radar on 10 January 2300-2359 UTC and 11 January 0000-0059 UTC, respectively. These plots reveal the complex patterns of the echo tops which are likely smoothed out by the lower resolution of the GOES imagery. The reflectivity structures evident between 5 and 8 km shown in Fig. 10 are suggestive of convective 'seeder' bands. They reoccurred at irregular time intervals of 2-5 minutes. The reflectivity structure at the same height is much more uniform during the next hour (Fig. 11). The average height of the 0 dBZ echo top is approximately 8 km during the 2-hour period. This height corresponds to 360 hPa which is within 20 hPa of the estimated cloud top pressure during that period. The profiles of reflectivity in these figures also indicate a strong vertical gradient of reflectivity between 3-5 km (550-700 hPa) which may be indicative of the process of dendritic crystal growth by deposition near the top and aggregation of falling crystals below.

ii) Moderate Snow event in Goose Bay

A prolonged moderate snow event affected Labrador on 6 April 2014. The location of surface instrumentation was near the Goose Bay international airport. A sequence of GOES-13 infrared satellite images with divergence at 300 hPa and satellite winds is shown in Fig. 12. During this period, the coldest cloud-tops with the most intense divergence passed over Newfoundland well to the southeast of Labrador. However, the satellite winds revealed the development of a cyclonic circulation and upper level trough (around 400 hPa) by 1815 UTC in southern Labrador. This feature moved east and was accompanied by enhanced upper level divergence during that time. Snow began around 03 UTC at the two measurement locations (Fig. 13). Continuous snowfall was primarily between 06-12 and 17-23 UTC. Mean precipitation rates (water equivalent) over 10-minute intervals were generally less than 1 mm hr^{-1}.

The horizontal divergence at 300 hPa inferred from GOES winds (Fig. 14) became positive near the time of onset continuous snowfall (06 UTC). Peak values occurred between 11-17 UTC. Precipitable water retrieved from the ground-based microwave radiometer (Fig. 15) was relatively constant between 00 and 15 UTC, followed by a small downward trend . The integrated cloud water (liquid water path) estimated from the microwave radiometer (Fig. 15) was nearly constant during the first period of precipitation. The second continuous period of snowfall occurred 2-3 hours after the onset of a significant increase in integrated cloud water at 13 UTC. The cloud water then remained nearly constant after about 20 UTC.

The sequence of rawinsonde profiles (Fig. 16) indicated a deep saturated layer and dendritic ice growth zone throughout the period. During the observed period (00 UTC 06 April

to 00 UTC 07 April), the height of the dendritic ice growth zone decreased slightly (50 hPa). This is consistent with the trend of increasing P(-15) and decreasing 600 hPa temperature inferred from GOES cloud top temperature and pressure (not shown) during the same period. The soundings suggest a separate thin cloud layer just above the deep saturated layer which lowered from 450 to 550 hPa in the first 12 hours of the period. Spatial variation in CTOP in the sampling box around Goose Bay was relatively large during this period. By 00 UTC 07 April, CTOP was more uniform and had increased in height to 450 hPa. The deep saturated layer extended up to this pressure level with no evidence of a thin cloud layer above. The GOES retrieved CTOP and DGZ top values appear to be within 50 hPa of the values observed in the soundings.

Cloud-top properties retrieved from the GOES DCOMP algorithm at 1845 UTC are given in Figs. 17-19. Corresponding time series near Goose Bay are shown for particle effective radius and optical depth (Fig. 20). At 1845 UTC, a band of ice clouds were present over central Labrador on the northwest side of the cyclonic circulation which developed around that time. This cloud area appeared to be associated with larger particle sizes and smaller optical depths than surrounding cloud areas. Relatively large spatial variability in these parameters was observed. The time trends in cloud type (not shown) indicate that a larger fraction of cloud tops consisted of supercooled particles between about 5-15 UTC (during the first precipitation event) than at later times. After 15 UTC, the cloud tops were dominated by ice crystals.

The retrievals of effective radius and optical depth were limited to 1000-2300 UTC when solar elevation angle was sufficient to be used for the retrievals. There was a distinct upward trend in particle size during the transition to all ice particles (1200-2300 UTC). This was during the second period of continuous precipitation. The optical depth generally appears uncorrelated

with the effective radius during this period. Optical depth maxima occurred at around 11, 14-17, and 22 UTC. The decrease in optical depth from 1100 to 1300 UTC and from 1300 to 1700 UTC may be attributed in part to the shift from liquid to ice phase in the cloud tops, and increasing ice particle sizes, respectively. Relationships between the observed precipitation and factors such as cloud top ice/liquid fraction, effective radius and optical depth are unclear from these data alone.

The SCaMPR algorithm did not detect precipitation in the vicinity of Goose Bay during 06 April 2014. Apparently, the cloud top temperatures were warmer than the threshold used to flag precipitation in the algorithm. However, it should be noted that the rain / no rain separation in SCaMPR is calibrated using a threshold of 1 mm/h (Kuligowski et al. 2014), and since most of the precipitation rates during this event were below 1 mm/h, it is not entirely surprising that SCaMPR missed the precipitation during this particular event.

5. Discussion and Conclusions

Without additional information, visible and infrared satellite observations have limited ability to determine the conditions within and below clouds. Nevertheless, the imagery from geostationary satellites is invaluable given their ability to provide high temporal sampling and widespread coverage in remote areas lacking ground-based radars. Indeed, imagery from such satellites has gained widespread use by meteorologists along with other observations and models in the forecast arena. The importing findings from the present work are summarized below.

The quantitative measures of cloud top properties, cloud top pressure and temperature, were used to estimate internal temperature within the cloud layer, and the height where the dendritic ice growth process might be active. However, additional information is required to

determine if saturation and lift are present at this height. In strong winter storms, such as the one which affected Newfoundland on 10-11 January 2013, it appears that upper-level divergence derived using satellite-based wind observations may be useful as a proxy for deep layer saturation and upward air motion in the middle layers of the troposphere.

The results shown here suggest that SCaMPR, or similar algorithms which combine visible/infrared observations with microwave retrievals, may provide useful estimates of precipitation rates in strong winter storms. However additional work will be needed to adjust and validate these algorithms for frozen precipitation using a much larger sample of events than were presented in this study. Perhaps a statistical approach will be needed to best combine the different sources of information described here into a single tool for determining probabilities of frozen precipitation amounts.

While it is hoped that the cloud top properties examined in this paper may be useful to identify areas with the potential for heavy snowfall where ground based radar is lacking, several limitations exist. The profile of temperature in the lower troposphere is extremely important in determining the type of precipitation reaching the surface: rain, freezing rain, ice pellets or snow. For example, the existence of a warm layer below 700 hPa could result in melting of snow falling from above. A cold layer near the surface could then lead to freezing of the melted snow into ice pellets, or freezing rain reaching the surface, depending on the cold layer thickness.

The retrieval of the temperature profiles in the lower layers of clouds and sub-cloud layer is not possible from satellite-based infrared observations.   Perhaps, microwave retrievals from instruments such as the Advanced Microwave Sounding Unit (AMSU) aboard polar orbiting

satellites will be useful in this regard (L<small>IU AND</small> W<small>ENG</small>, 2005; B<small>OUKABARA</small> et al. 2011). However, vertical resolution of the microwave retrieved sounding is limiting factor.

The use of cloud top information to detect light snowfall at the surface may not be possible. For example, snow is often produced from modest rising air motion associated with factors such as thermal advection in layers below 700 hPa. These processes may be undetected from cloud tops at higher altitudes.

The ability of the ground-based microwave radiometer to detect the onset of precipitation from retrieved "cloud water" was shown in this study. This suggests that additional cloud profile information from MIRS could also be combined with GOES data, much like microwave precipitation retrievals are currently being used as input to SCaMPR. This integration can significantly improve winter storm detection and its precipitation amount.

References

AUER, A. H., JR., AND J. M. WHITE, 1982: The combined role of kinematics, thermodynamics and cloud physics associated with heavy snowfall episodes. *J. Japan Met. Soc.,* **60,** 500-507.

BOUKABARA, S.-A., K. GARRETT, W. CHEN, F. ITURBIDE-SANCHEZ, C. GRASSOTTI, C. KONGOLI, R. CHEN, Q. LIU, B. YAN, F. WENG, R. FERRARO, T. KLEESPIES, AND H. MENG., 2011: An All-Weather 1DVAR Satellite Data Assimilation and Retrieval System. *IEEE Trans. Geosci. Remote Sens.*, **49**, 9, 3249-3272.

GULTEPE, I., T. KUHN, M. PAVOLONIS, C. CALVERT, J. GURKA, G.A. ISAAC, A. J. HEYMSFIELD, P.S.K. LIU, B. ZHOU, R. WARE, B. FERRIER, J. MILBRANDT, B. HANSEN, AND B. BERNSTEIN, 2014: Ice fog in Arctic during FRAM-IF project: Aviation and nowcasting applications. *Bulletin of Amer. Met. Soc.*, **95**, 211–226.

GULTEPE, I., B. ZHOU, J. MILBRANDT, A. BOTT, Y. LI, A. J. HEYMSFIELD, B. FERRIER, R. WARE, M. PAVOLONIS, T. KUHN, J. GURKA, P. LIU, AND J. CERMAK, 015: A review on Ice Fog Measurements and Modeling. *Atmospheric Research*. **151**, 2-19.

HAYDEN, C.M., R. J. PURSER, 1995: Recursive filter objective analysis of meteorological fields, applications to NESDIS operational processing. *J. Appl. Meteor.,* **34**, 3-15.

HOU, A.Y., R. K. KAKAR, S. NEECK, A. A. AZARBARZIN, C. D. KUMMEROW, M. KOJIMA, R. OKI, K. NAKAMURA, AND T. IGUCHI, 2014: The Global Precipitation Measurement Mission. *Bull. Amer. Meteor. Soc.*, **95**, 701–722.

KADIN, C., 1982: The Minneapolis Snow Event -What Did The Satellite Imagery Tell Us? *National Wea. Digest*, **7**, 3, 13-16.

KULIGOWSKI, R.J., Y. LI, AND Y. ZHANG, 2013: Impact of TRMM data on a low-latency, high-resolution precipitation algorithm for flash-flood forecasting. *J. Appl. Meteor. Cli.*, **6**, 1379-1393.

LIU, Q., AND F. WENG, 2005: One-dimensional retrieval algorithm of temperature, water vapor, and cloud water profiles from advanced microwave sounding unit (AMSU). *IEEE Geosci. Remote Sensing*, **43**, 5, 1087-1095.

OLSON, W.S., C.D. KUMMEROW, G.M. HEYMSFIELD, L. GIGLIO, 1996: A method for combined passive-active microwave retrievals of cloud and precipitation profiles. *J. App. Meteor.*, **35**, 1763-1788.

RABIN, R.M., S.F. CORFIDI, J.C. BUNNER, C.E. HANE, 2004: Detecting winds aloft from water vapour satellite imagery in the vicinity of storms. *Weather*, **59**, 251-257.

RABIN, R.M., J. HANNA, 2008: GOES winter precipitation efficiency algorithm. *Fifth GOES Users Conference. American Meteorological Society*. P1.34.

RASMUSSEN, R.,M. DIXON, S. VASILOFF, F. HAGE, S. KNIGHT, 2003: Snow nowcasting using a real-time correlation of radar reflectivity wuth snow gauge accumulation. *J. Appl. Meteor.*, **42**, 20-36.

SCOFIELD, R. A., 1987: The NESDIS operational convective precipitation estimation technique. *Mon. Wea. Rev.*, **115**, 1773-1792.

SCOFIELD, R. A., AND R. J. KULIGOWSKI, 2003: Status and outlook of operational satellite precipitation algorithms for extreme-precipitation events. *Mon. Wea. Rev.*, **18**, 1037-1051.

STEIGERWALDT, H., 1986: Deformation zones and heavy precipitation. *Natl. Wea. Dig.,* **11:1**, 15-20.

VELDEN, C.S., C.M. HAYDEN, S. NIEMAN, W.P. MENZEL, S. WANZONG, AND J. GOERSS, 1997: Upper-tropospheric winds derived from geostationary satellite water vapor observations. *Bull. Amer. Meteor. Soc.*, **78**, 173-195.

VELDEN, C. S., J. DANIELS, D. STETTNER, D. SANTEK, J. KEY, J. DUNION, K. HOLMLUND, G. DENGEL, W. BRESKY, AND P. MENZEL, 2005: Recent Innovations in Deriving Tropospheric Winds from Meteorological Satellites. *Bull. Amer. Meteor. Soc.*, 86, 205-223.

VICENTE, G. A., R. A. SCOFIELD, AND W. P. MENZEL, 1998: The operational GOES infrared rainfall estimation technique. *Bull. Amer. Meteor. Soc.*, **79**, 1883- 1898.

WALTHER, A., AND A.K. HEIDINGER, 2012: Implementation of the Daytime Cloud Optical and Microphysical Properties Algorithm (DCOMP) in PATMOS-x. *Journal of Applied Meteorology and Climatology*. **51**, 1371-1390.

WETZEL, S.W., AND J. E. MARTIN, 2001: An Operational Ingredients-Based Methodology for Forecasting Midlatitude Winter Season Precipitation. *Wea. Forecasting*, **16**, 156–167.
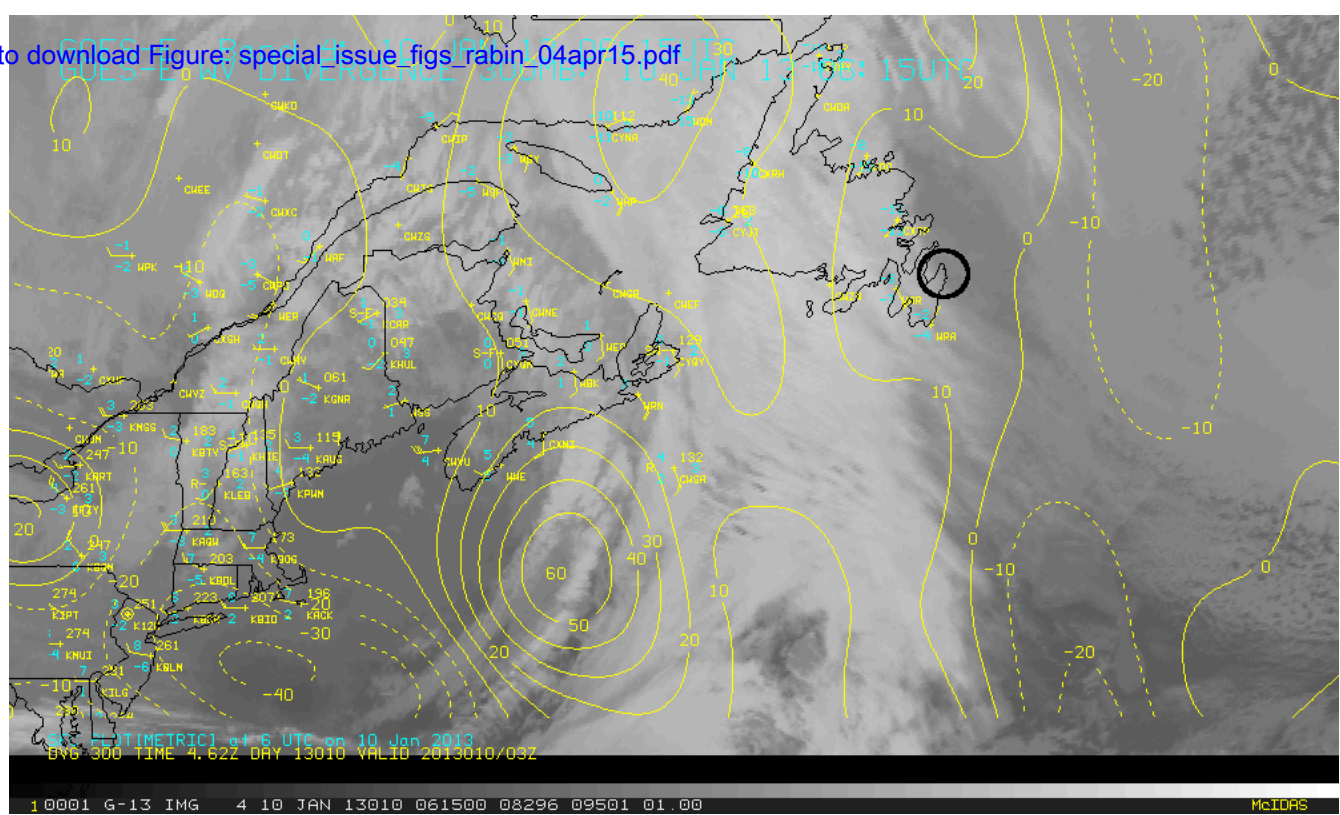
Figure 1a: GOES-13 infrared imagery (11.7 micron) 10 January 2013 0615 UTC. Surface weather observations (yellow and cyan) and horizontal divergence at 300 hPa (yellow contours) are plotted. Approximate location of ground-based sensors near St John's, NL is indicated by the circle.
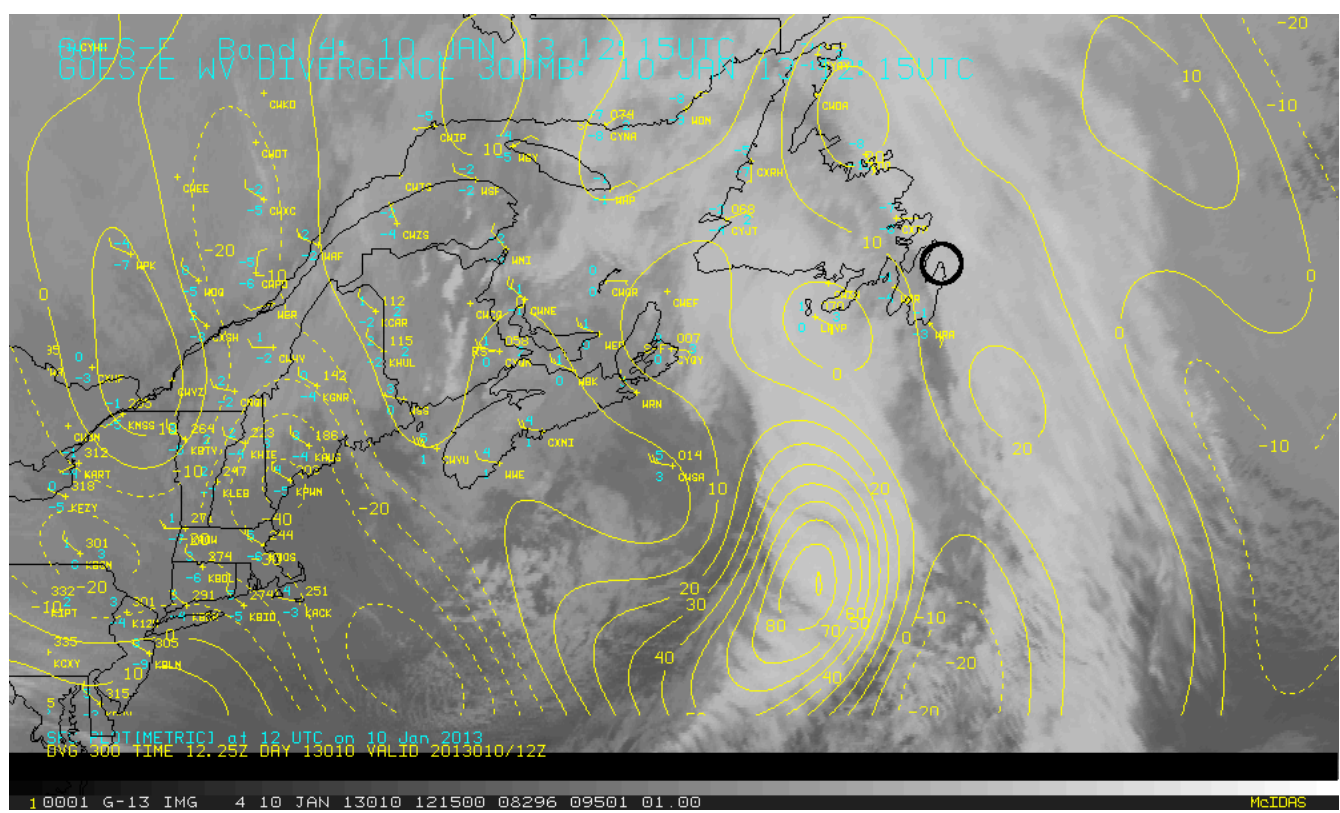
Figure 1b: Same as Fig. 1a except for 10 January 2013 1215 UTC.
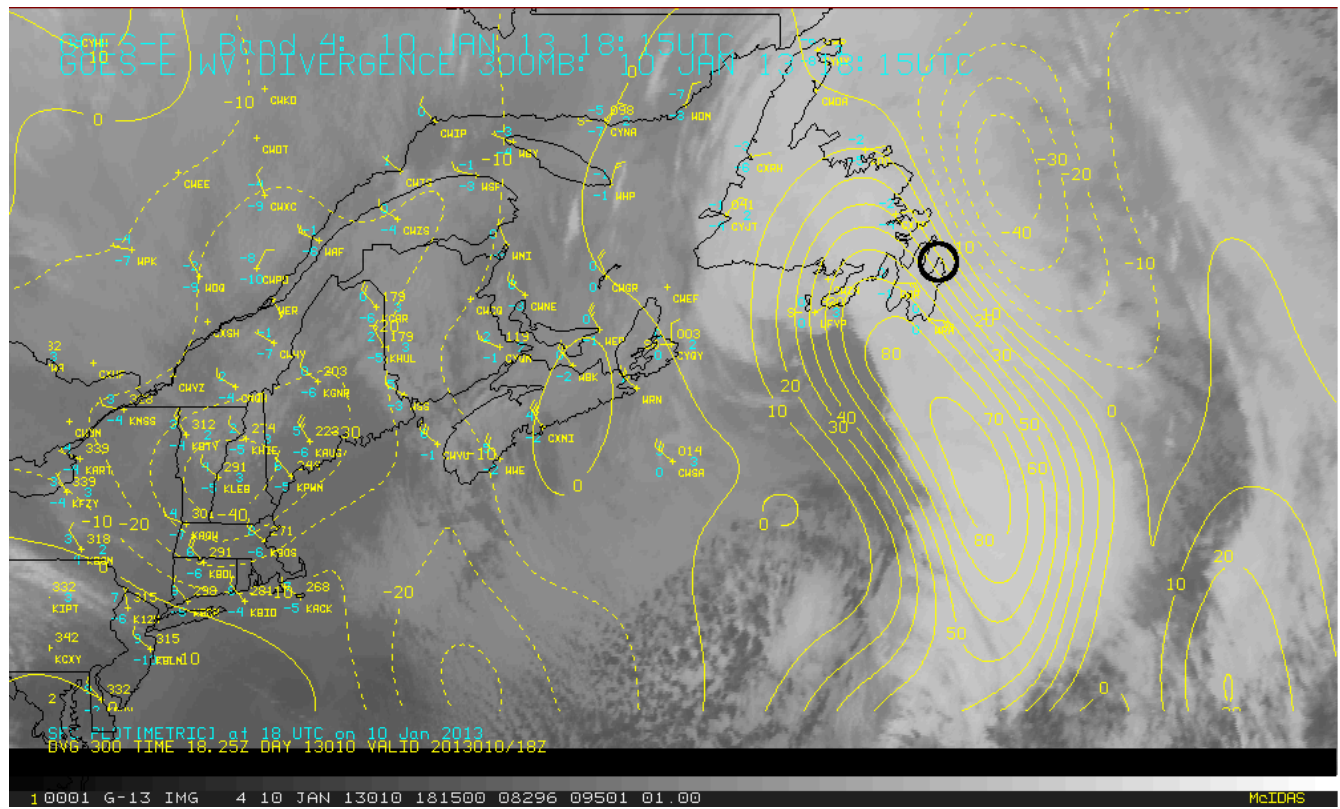
Figure 1c: Same as Fig. 1a except for 10 January 2013 1815 UTC.
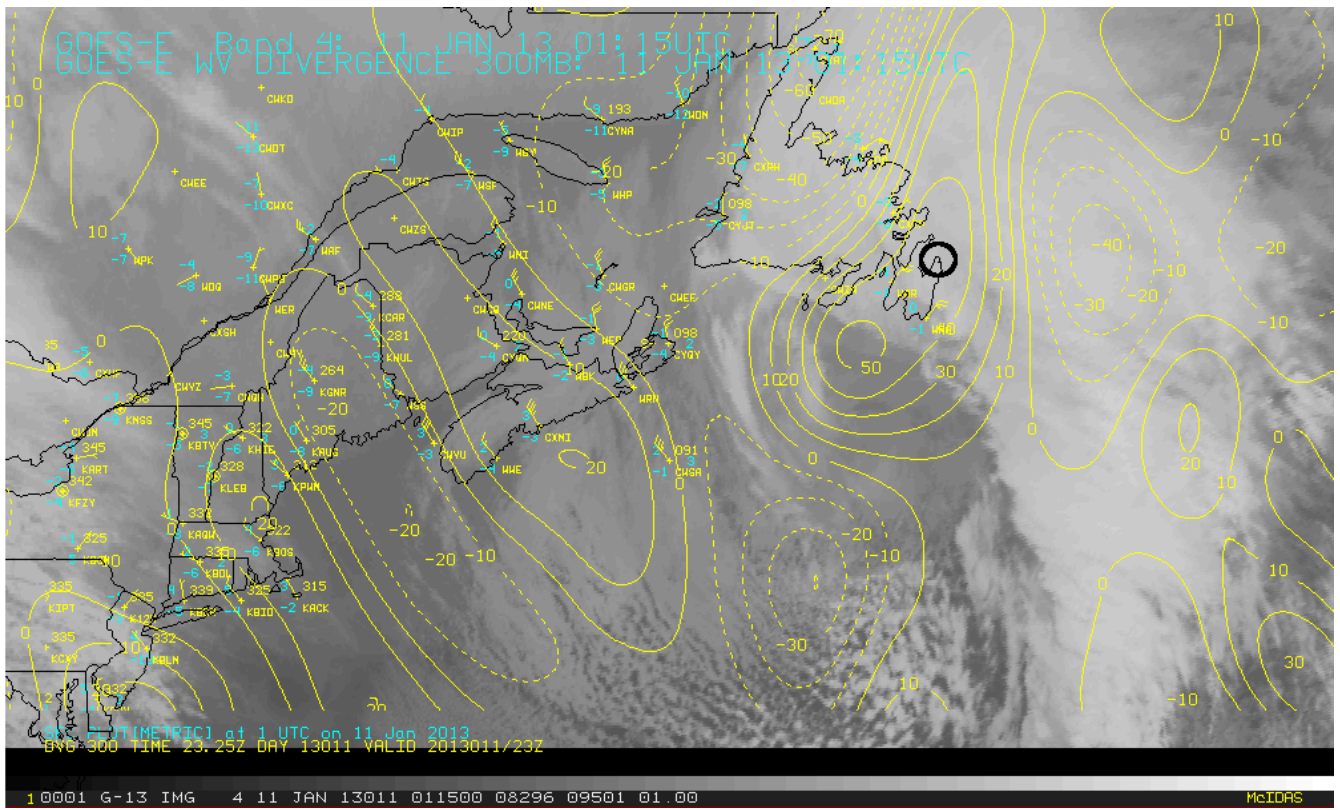
Figure 1d: Same as Fig. 1a except for 11 January 2013 0115 UTC.
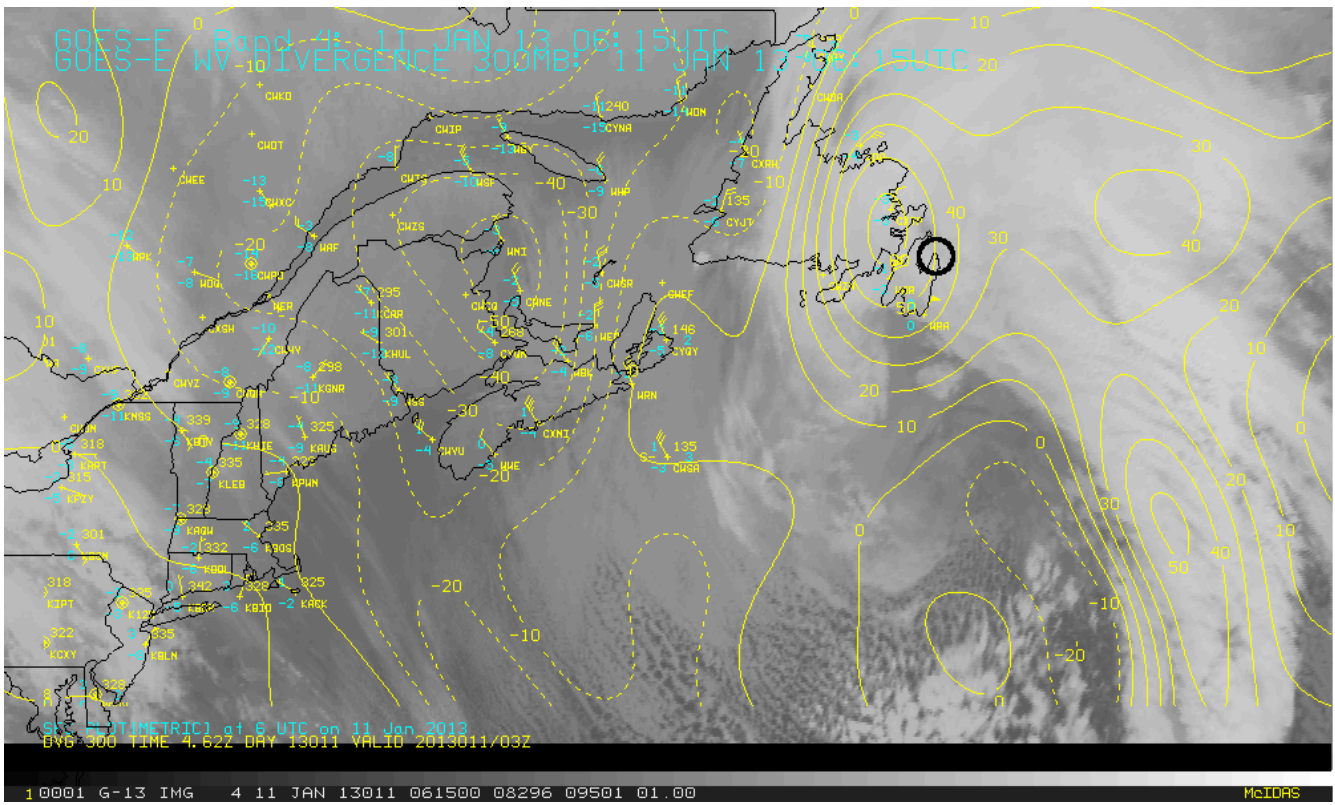
Figure 1e: Same as Fig. 1a except for 11 January 2013 0615 UTC.
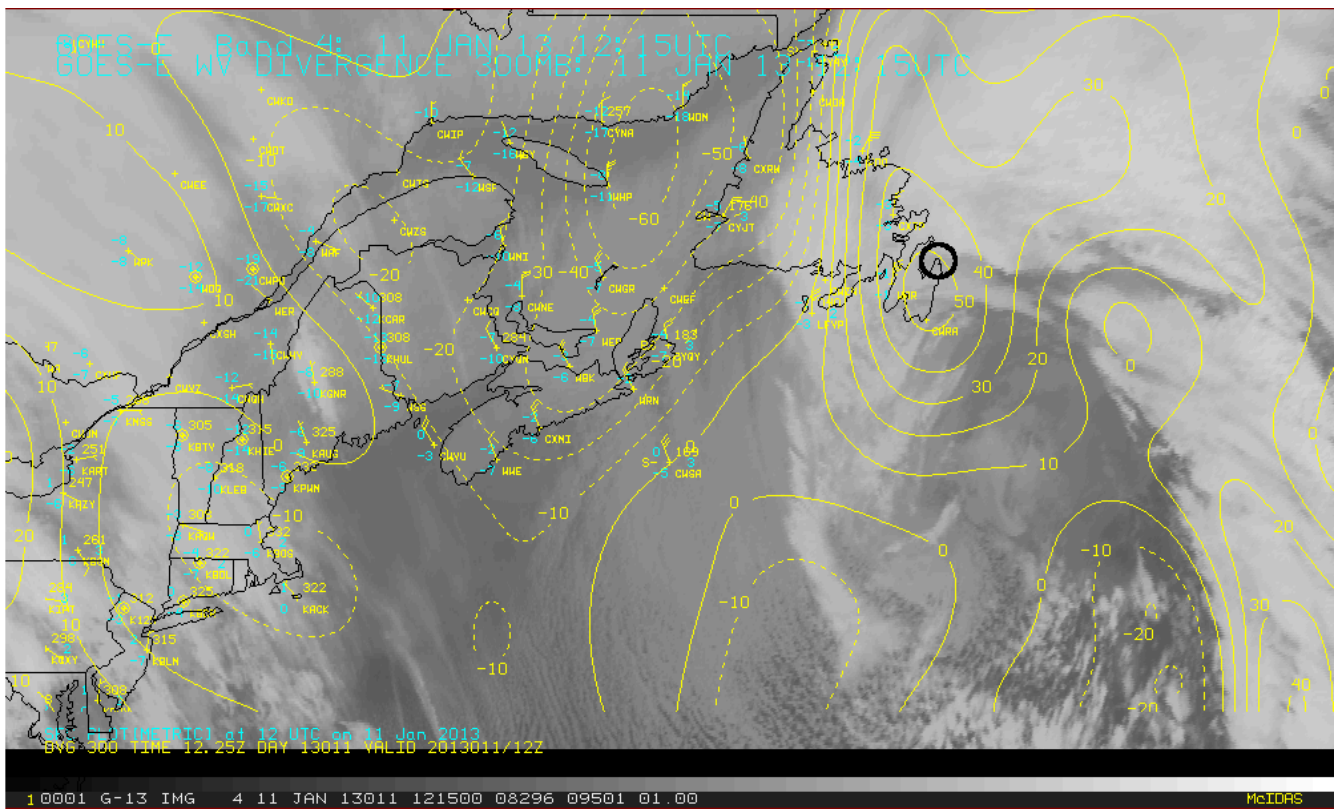
Figure 1f: Same as Fig. 1a except for 11 January 2013 1215 UTC.

Figure 1g: Same as Fig. 1a except for 11 January 2013 1815 UTC.
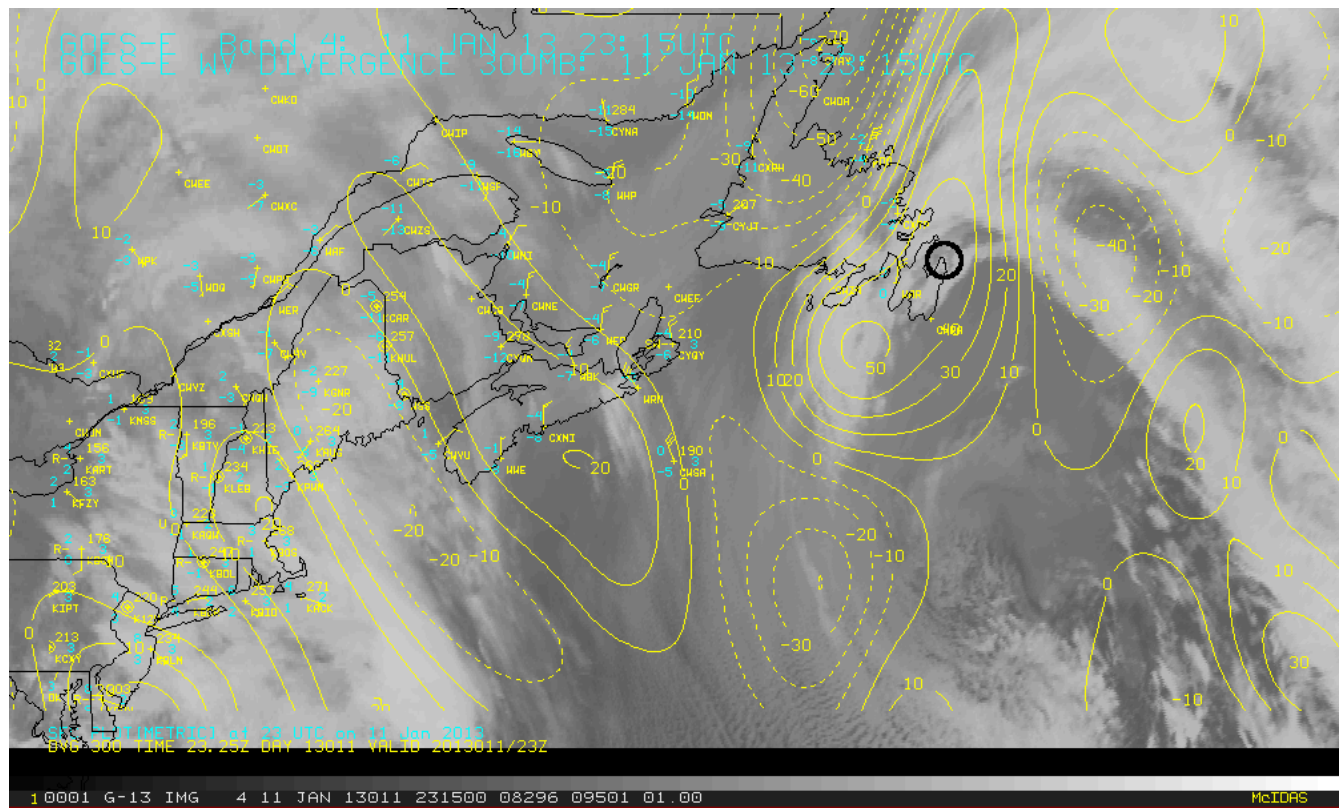
Figure 1h: Same as Fig. 1a except for 11 January 2013 2315 UTC.
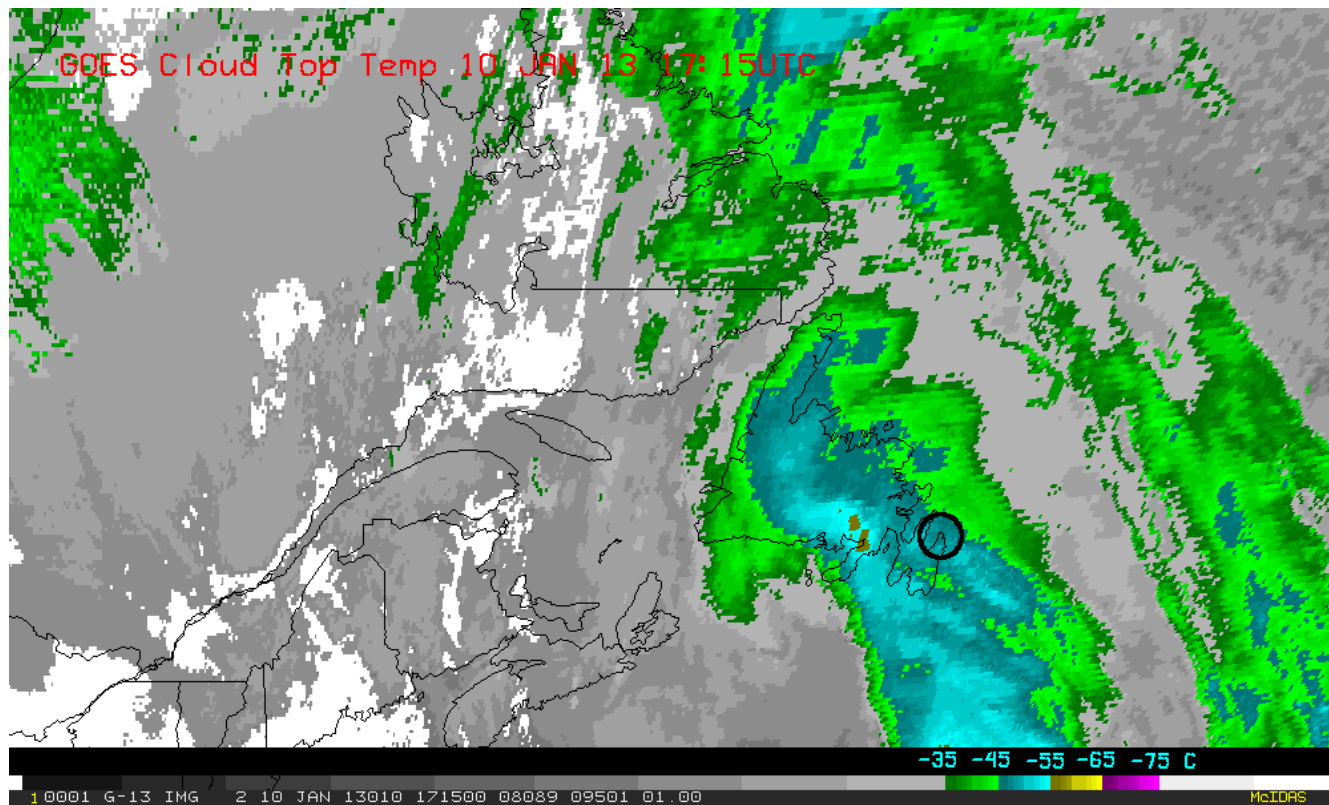
Figure 2a. Cloud top temperature, 1815 UTC 10 January 2013. Approximate location of ground-based sensors near St John's, NL is indicated by the circle.
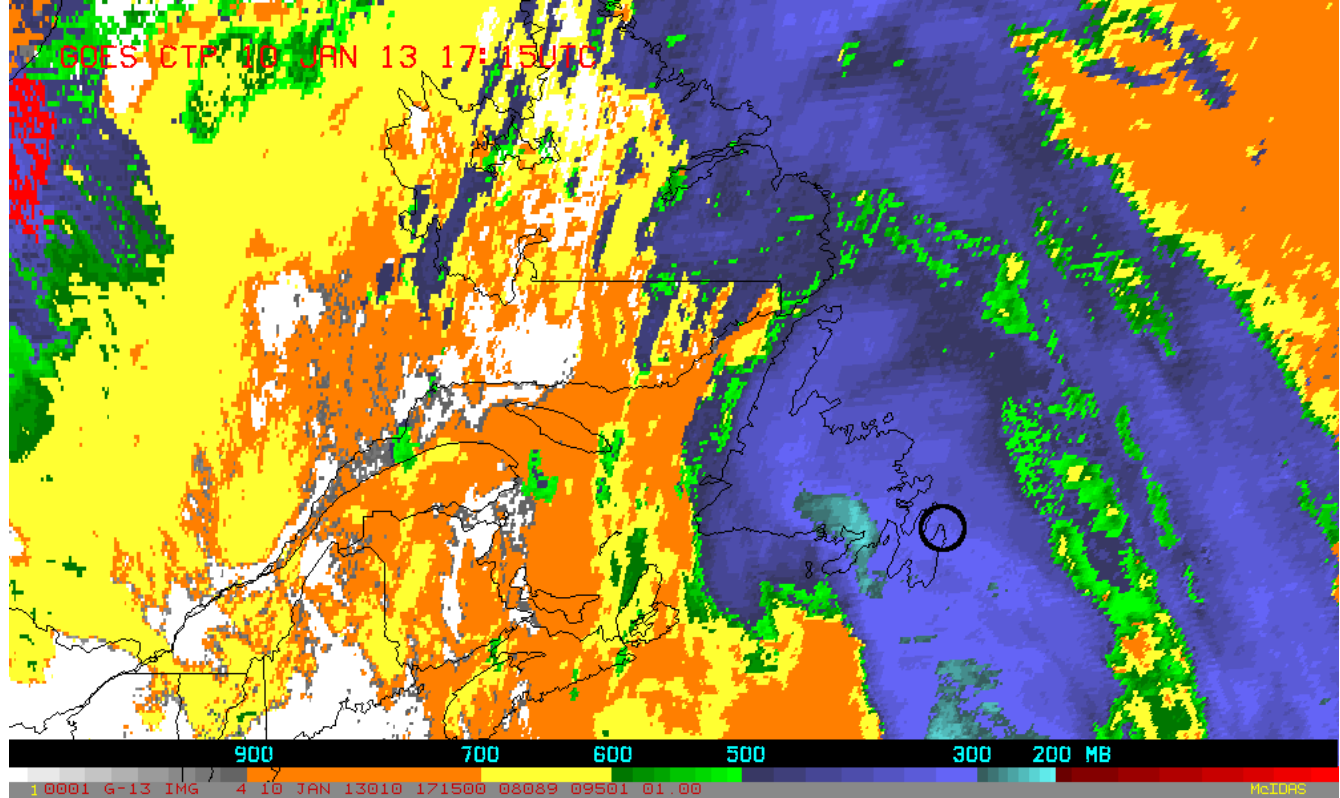
Figure 2b. Same as Fig. 2a except for Cloud Top Pressure (hPa).
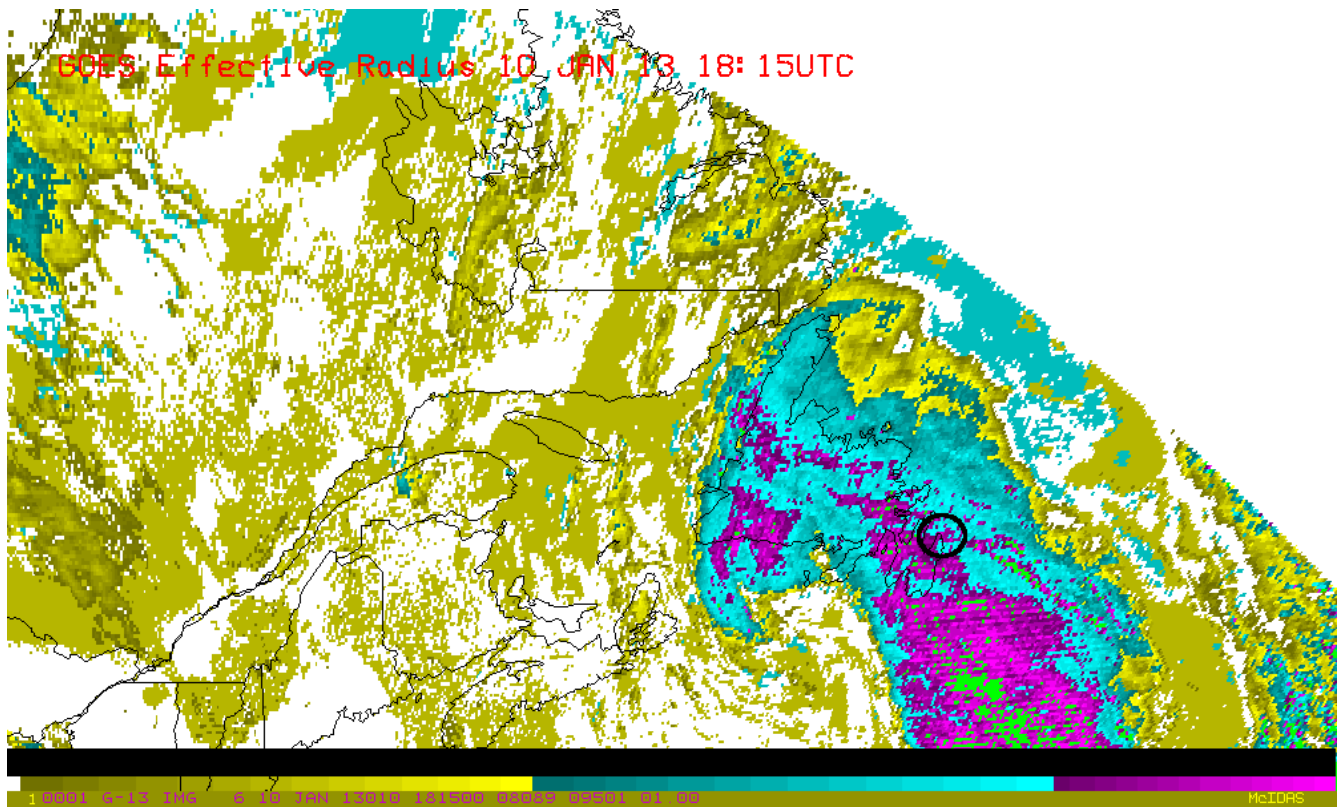
Figure 2c. Same as Fig. 2a except for effective cloud top particle radius (yellow=small;cyan=medium;violet=large).
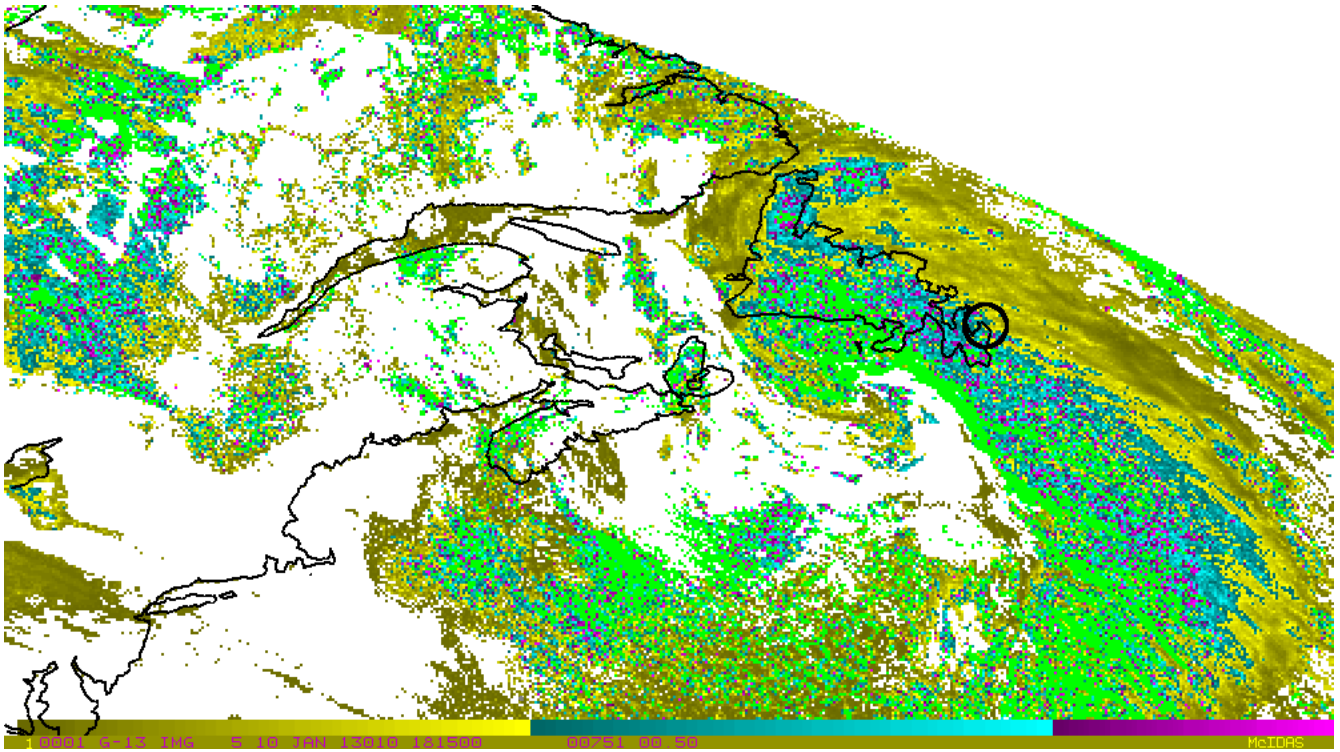
Figure 2d. Same as Fig. 2a except for cloud optical depth (yellow=small;cyan=medium;violet, green=large).
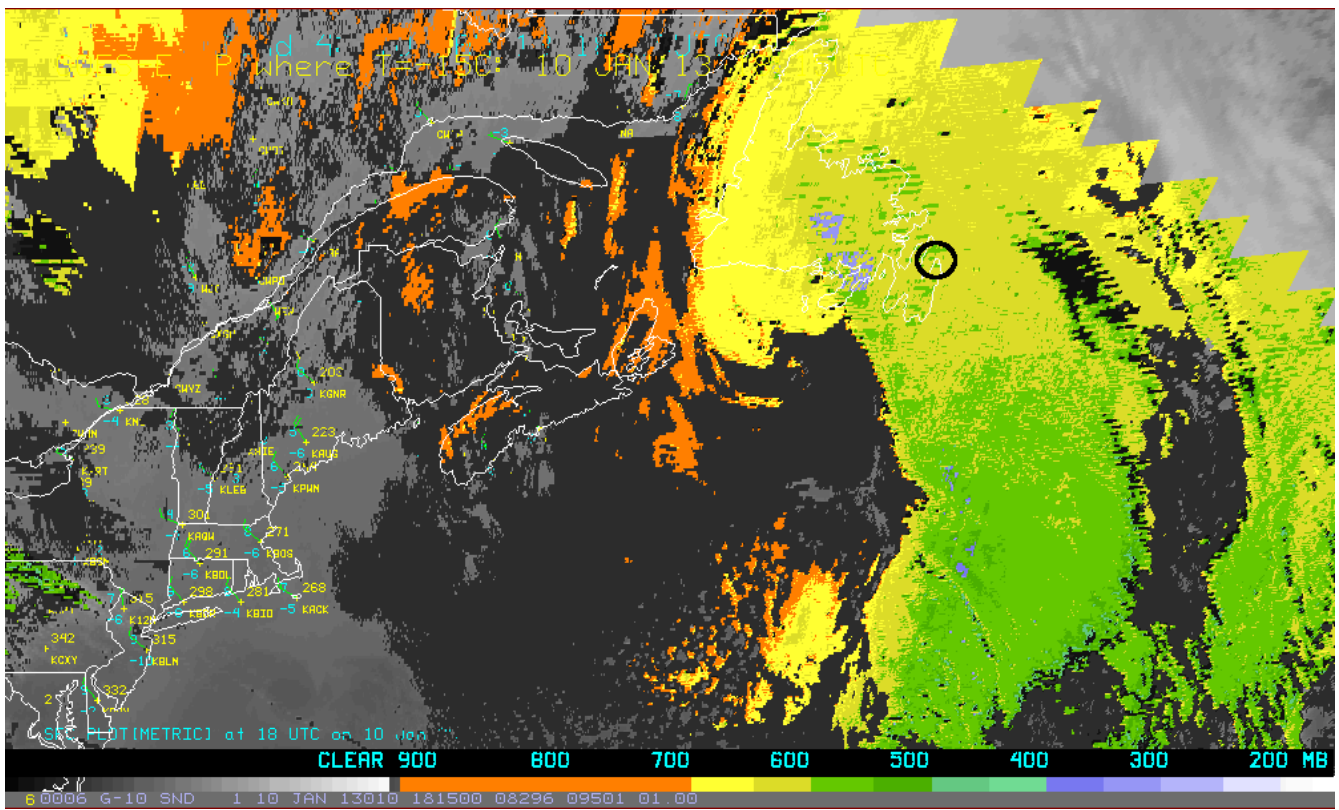
Figure 3a. Derived pressure of -15ºC isotherm, P(-15), 10 January 2013 1815 UTC. Approximate location of ground-based sensors near St John's, NL is indicated by the circle.
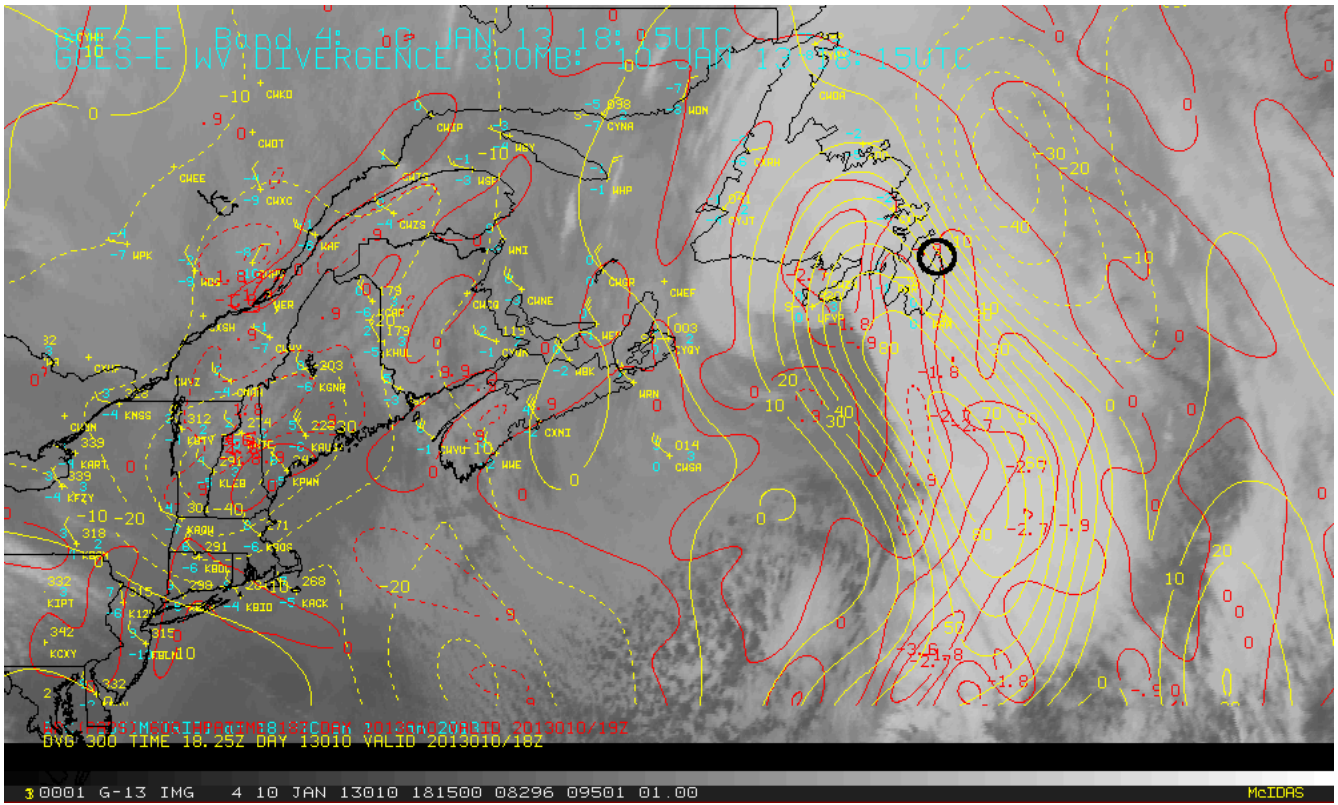
Figure 3b. Same as Fig. 3a. except for divergence at 300hPa (10^{-5} s^{-1} yellow contours) and vertical air motion at 600 hPa (omega, μb s^{-1} red contours). Positive (negative) divergence contours are solid (dashed). Upward (negative) air motion are solid (dashed).
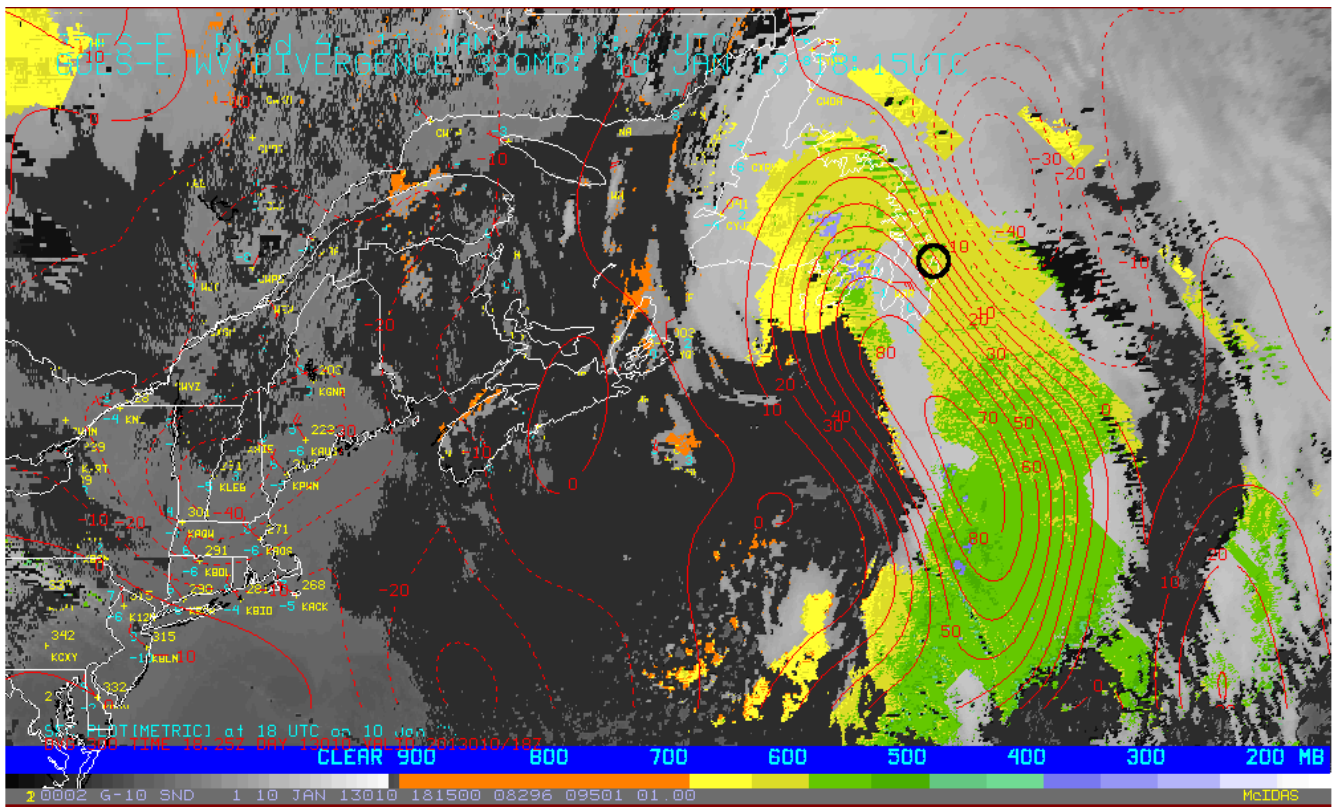
Figure 3c. Same as Fig. 3a. except for P(-15) with upward air motion threshold (omega less than -5 μb s^{-1}). Divergence at 300hPa is also shown (10^{-5} s^{-1} red contours).
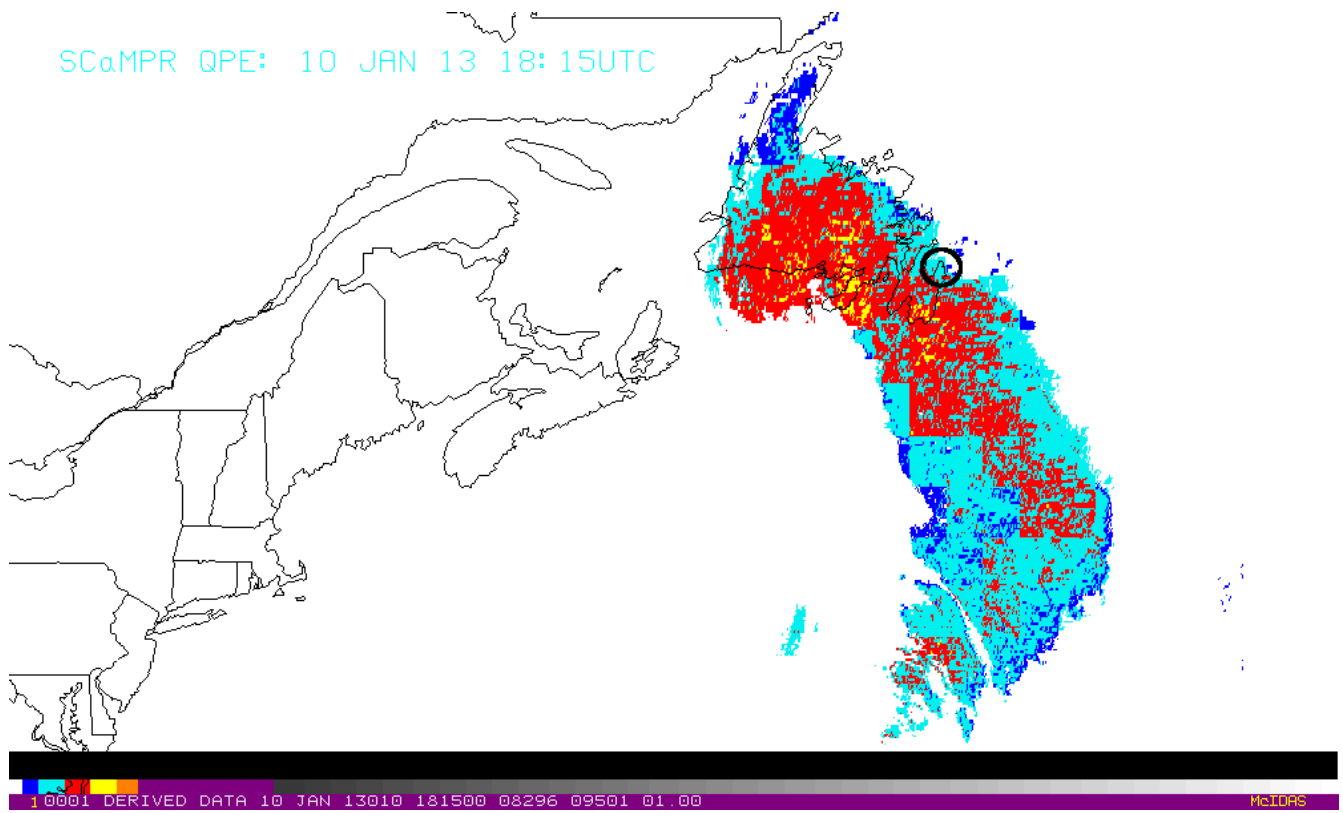
Figure 3d. Same as Fig. 3a. except for SCaMPR estimated precipitation rate. Red and yellow are greater than 2 and 3 mm h^{-1}, respectively.
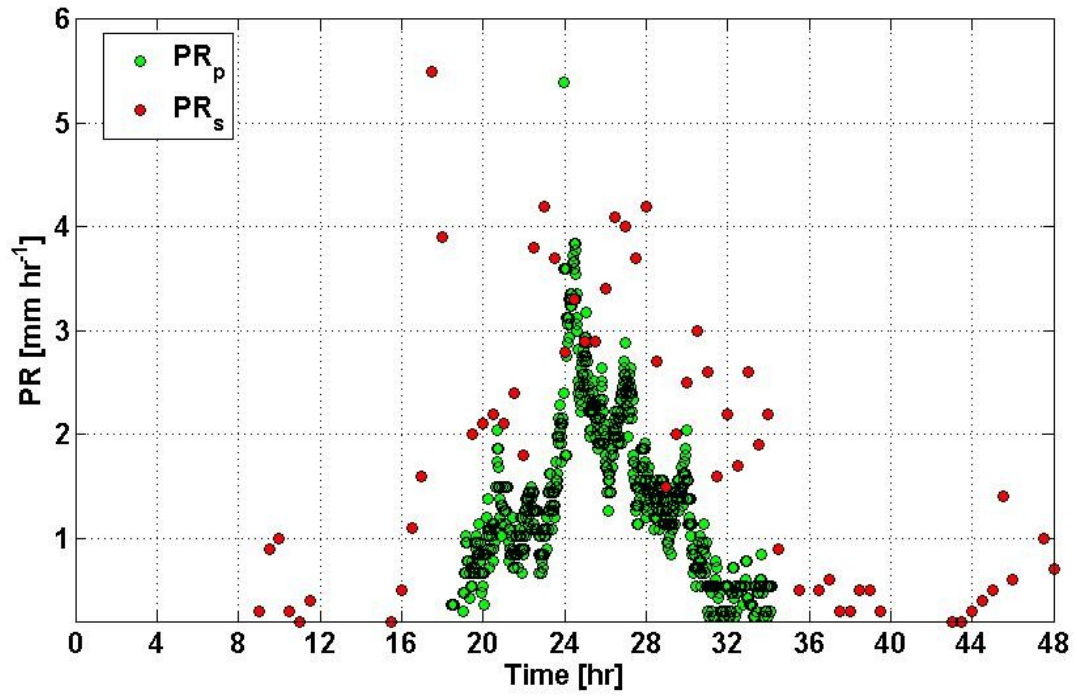
Figure 4. Precipitation rate on 10-11 January 2013 from pluviometer (green), SCaMPR (red). Times are hours since 10 January 00 UTC.
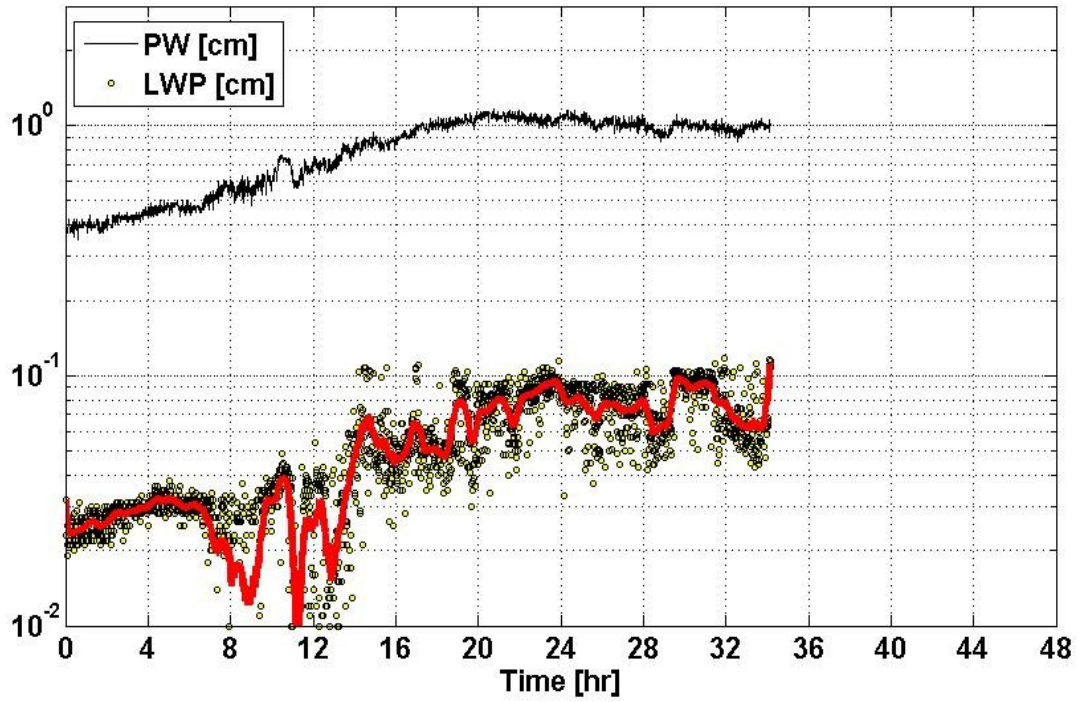
Figure 5. Integrated Precipitable Water (PW) and Liquid Water Path (LWP) on 10-11 January 2013. Times are hours since 10 January 00 UTC.
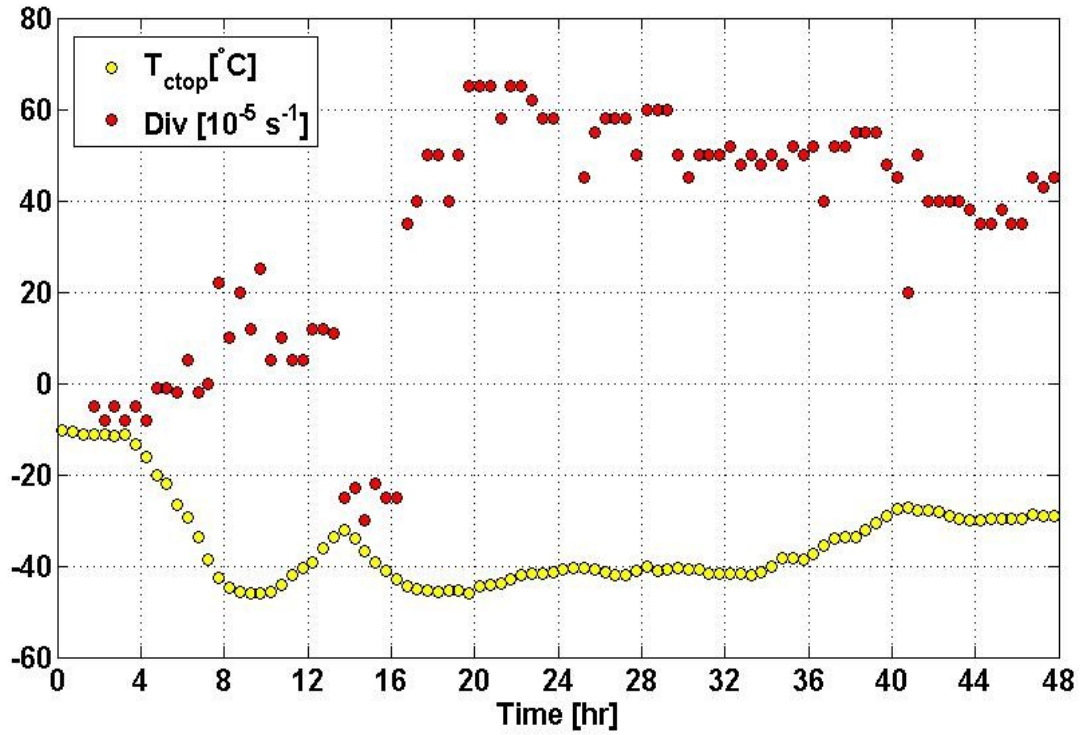
Figure 6. Divergence at 300 hPa and cloud top temperature on 10-11 January 2013. Times are hours since 10 January 00 UTC.
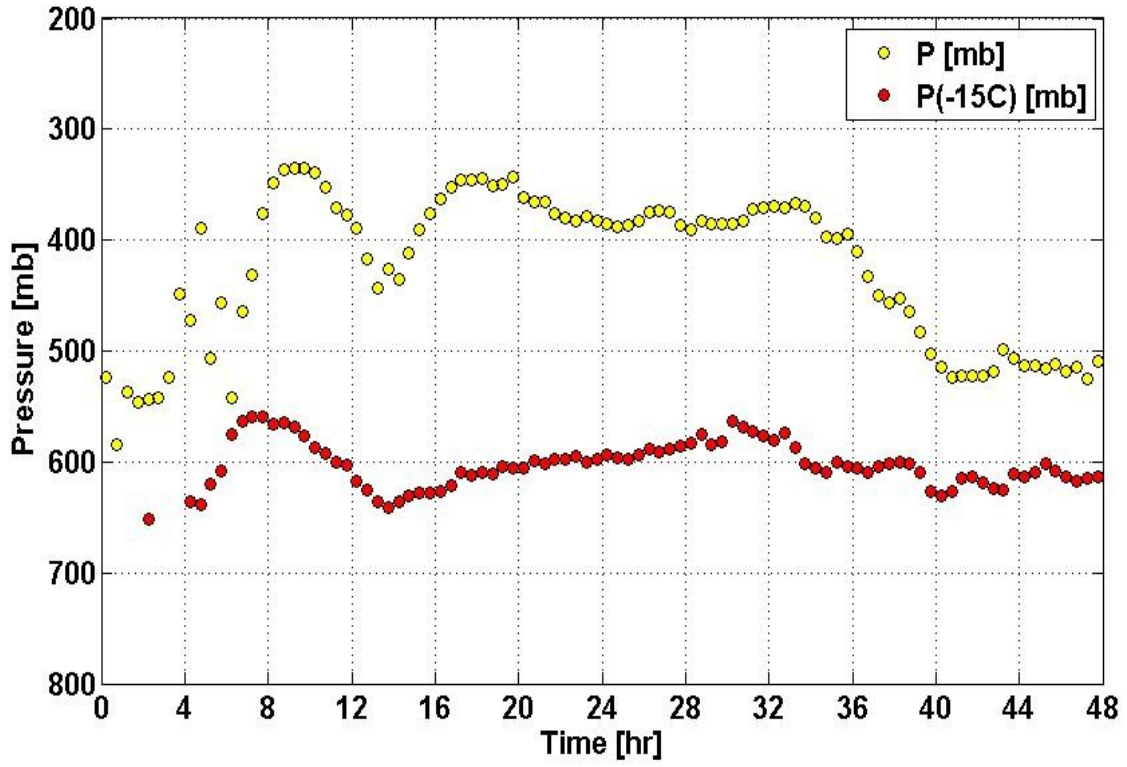
Figure 7. Cloud top pressure and P(-15) on 10-11 January 2013. Times are hours since 10 January 00 UTC.
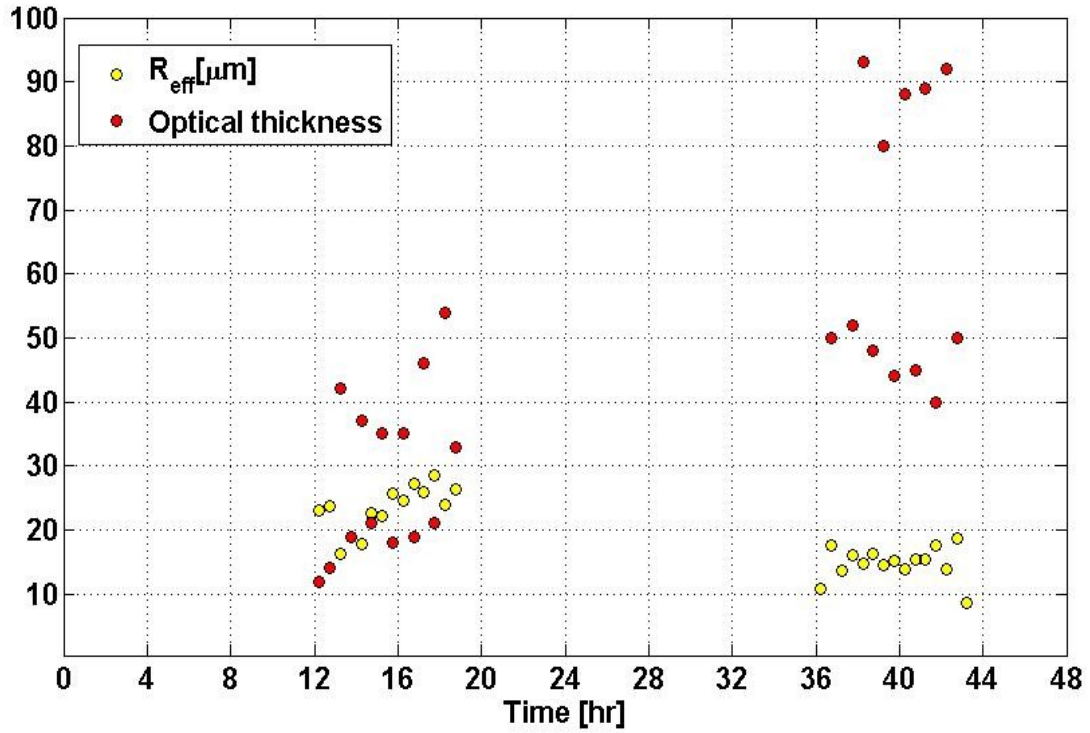
Figure 8. Cloud top effective radius and optical depth on 10-11 January 2013. Times are hours since 10 January 00 UTC.
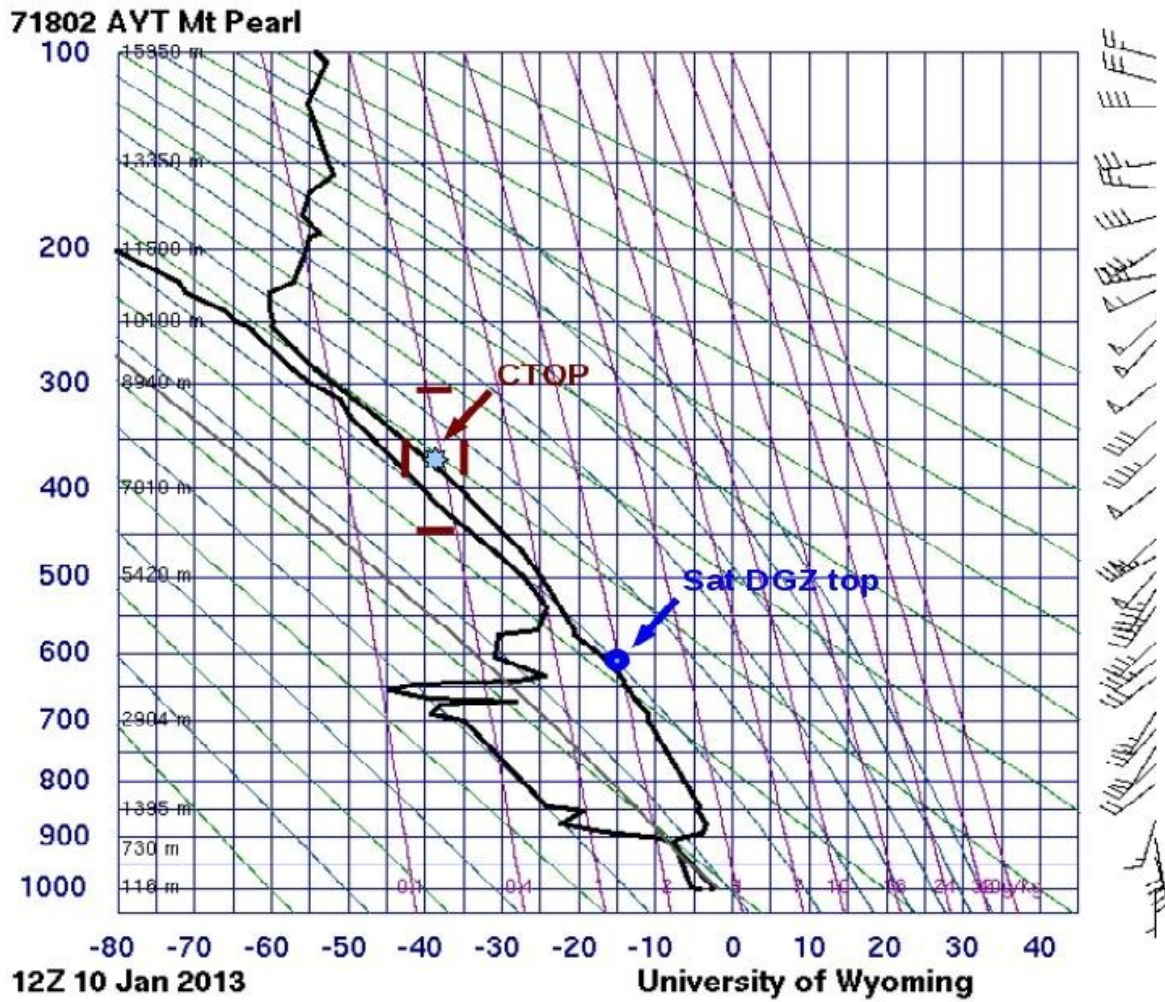
Figure 9a. Observed rawinsonde plots 10 January 12 UTC near St Johns. Estimated cloud top from GOES (CTOP) with uncertainties in temperature and pressure. Top of dendritic ice growth zone from GOES (DGZ).
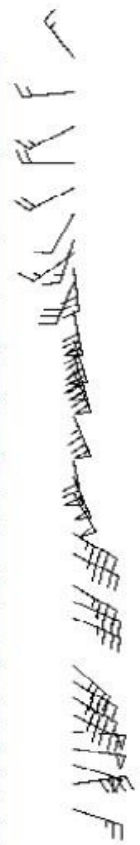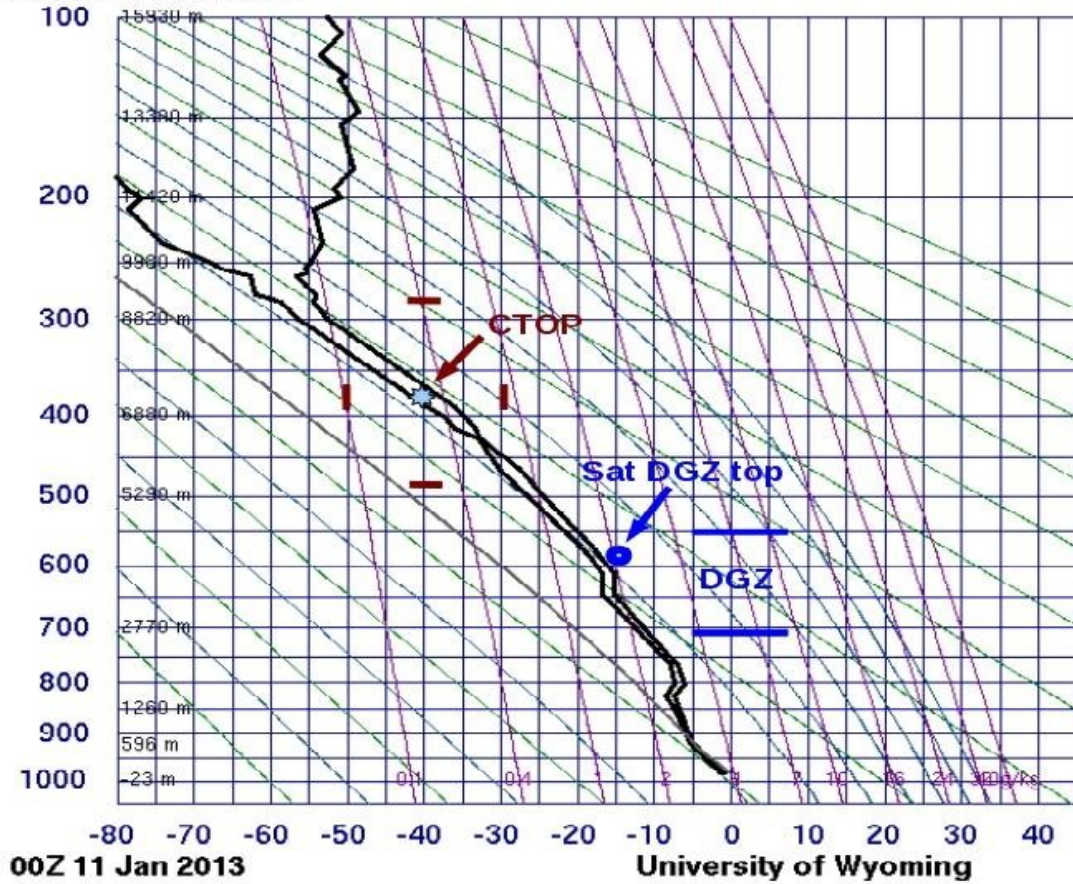
Figure 9b. Same as Fig. 9a except for 11 January 00 UTC.
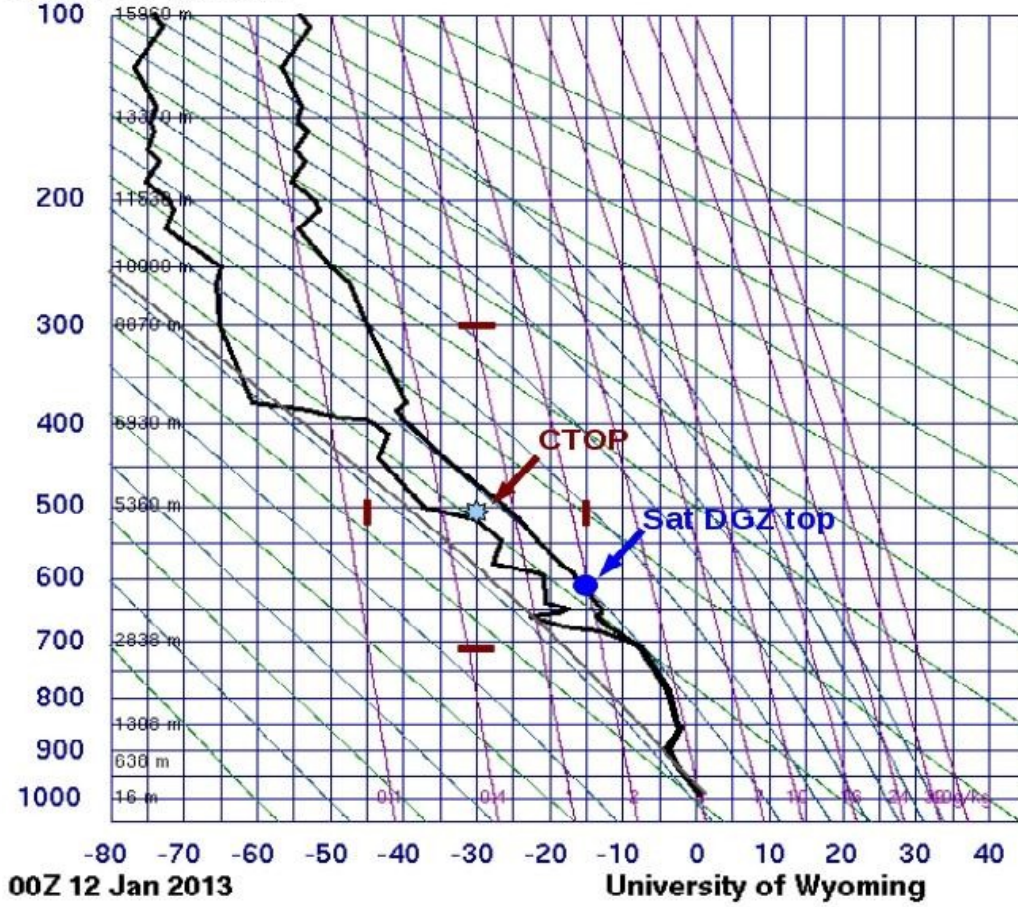
Figure 9c. Same as Fig. 9a except for 12 January 00 UTC.
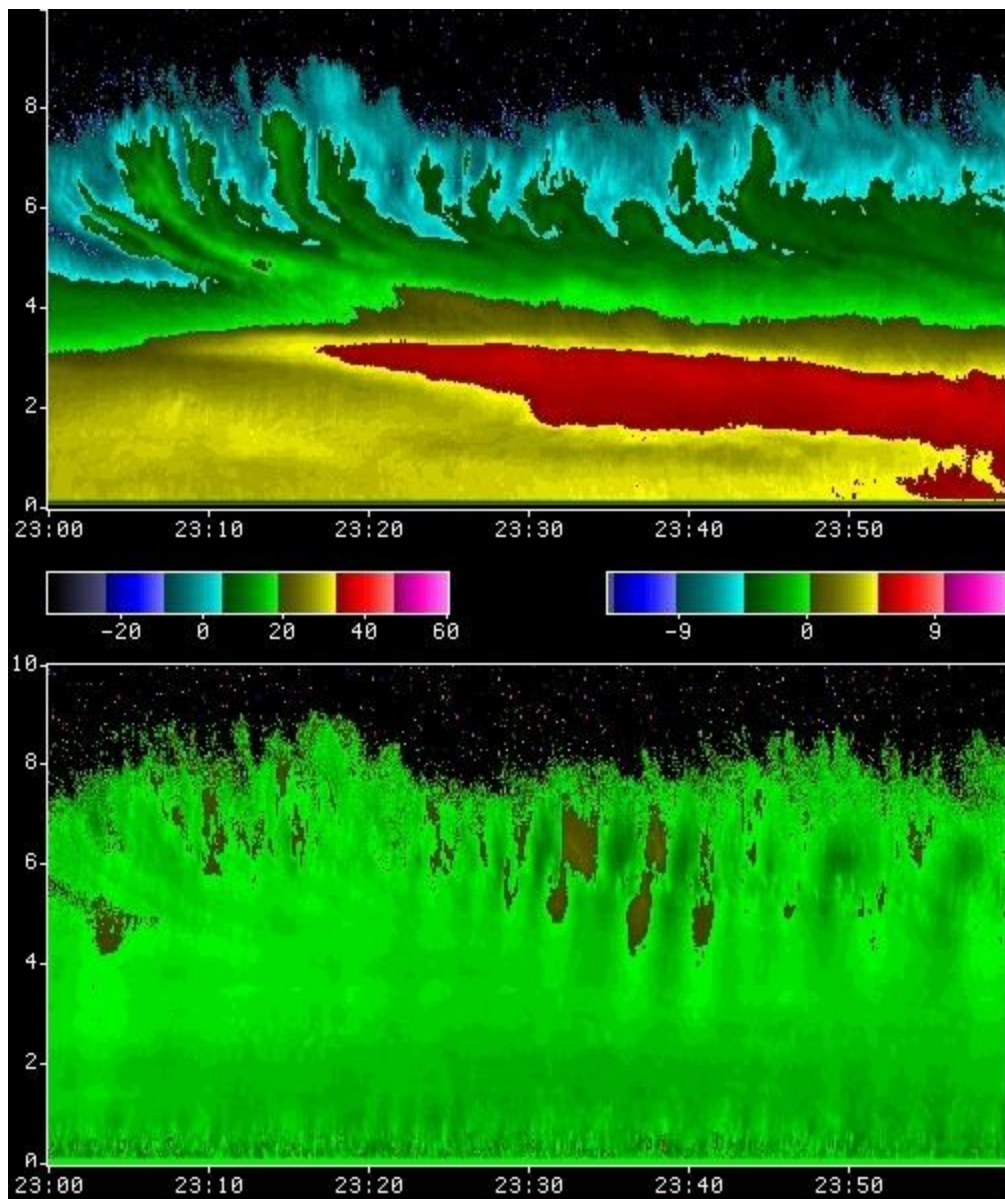
Figure 10. McGill X-band radar. Height-time display of reflectivity (dBZ, top) and vertical velocity (m s^{-1}, bottom). 10 January 2013, 2300-2359 UTC.
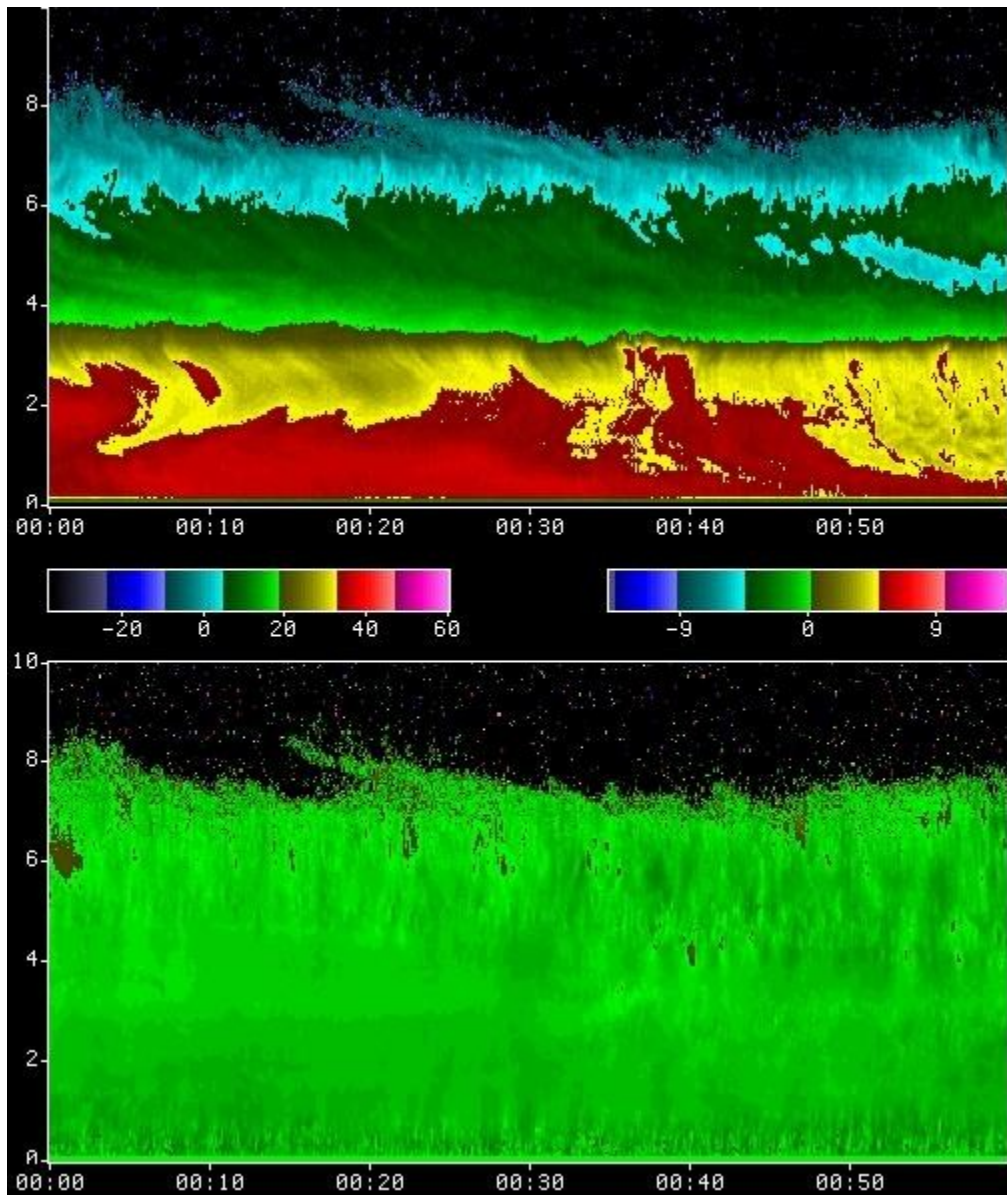
Figure 11. Same as Fig. 10 except for 11 January 2013, 0000-0059 UTC.
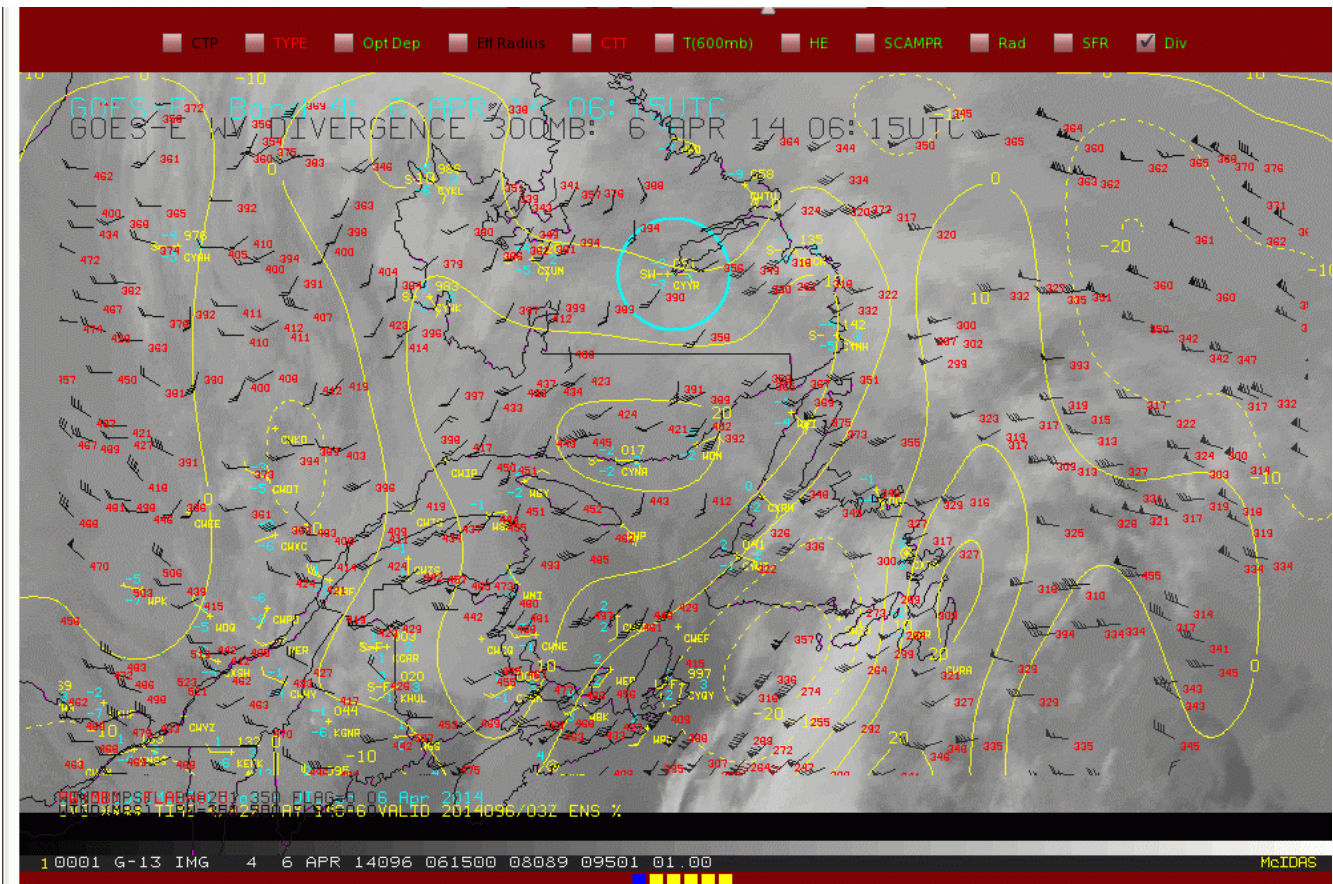
Figure 12a. GOES-13 infrared imagery (11.7 micron), surface weather observations (cyan and yellow), satellite winds (black wind barbs, pressure level in red, hPa) and contours of divergence at 300 hPa (contours in yellow, 10^{-5} s^{-1}) for 06 April 2014 06:15 UTC. The region surrounding Goose Bay, NL is circled.
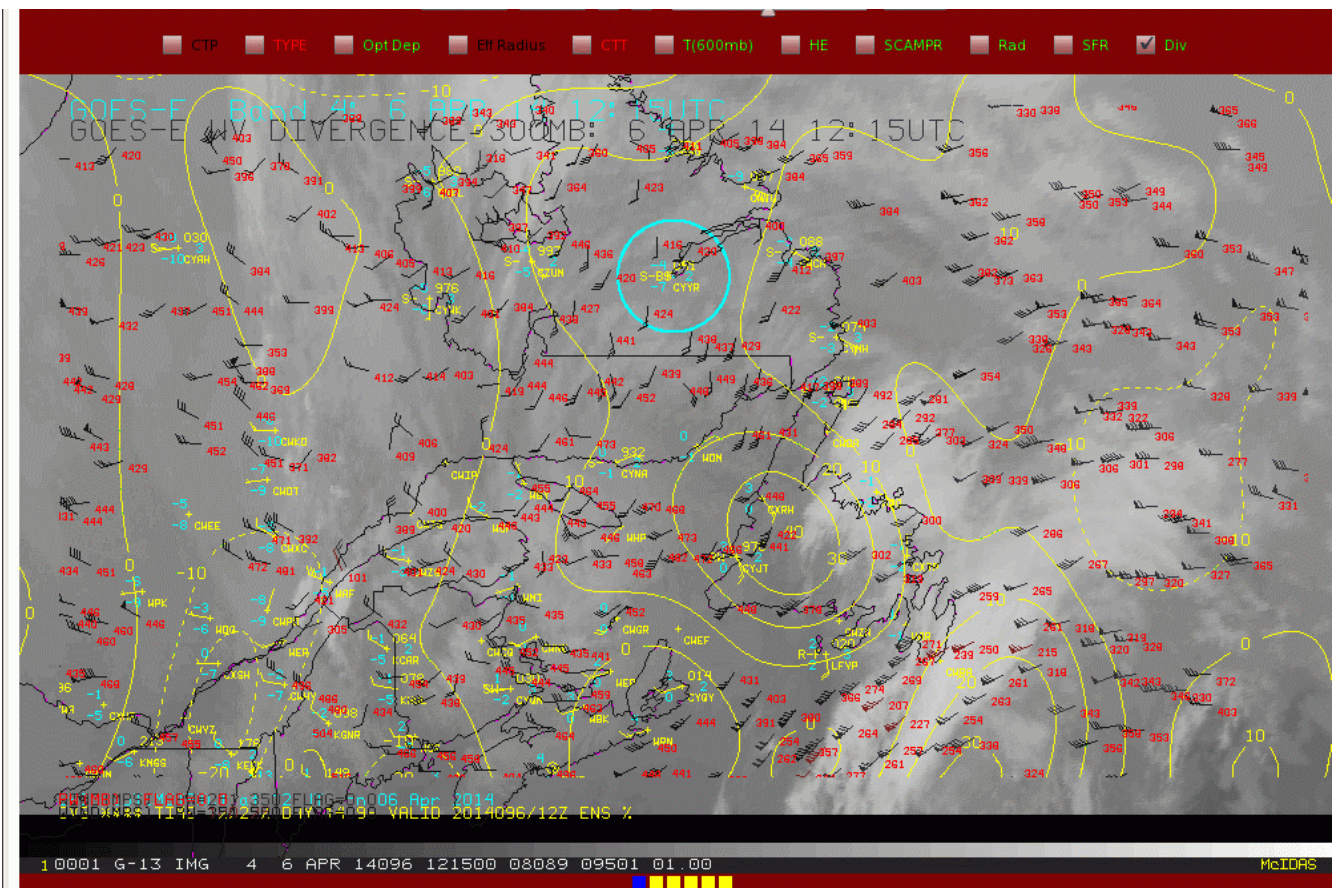
Figure 12b. Same as Fig. 12a except for 12:15 UTC.
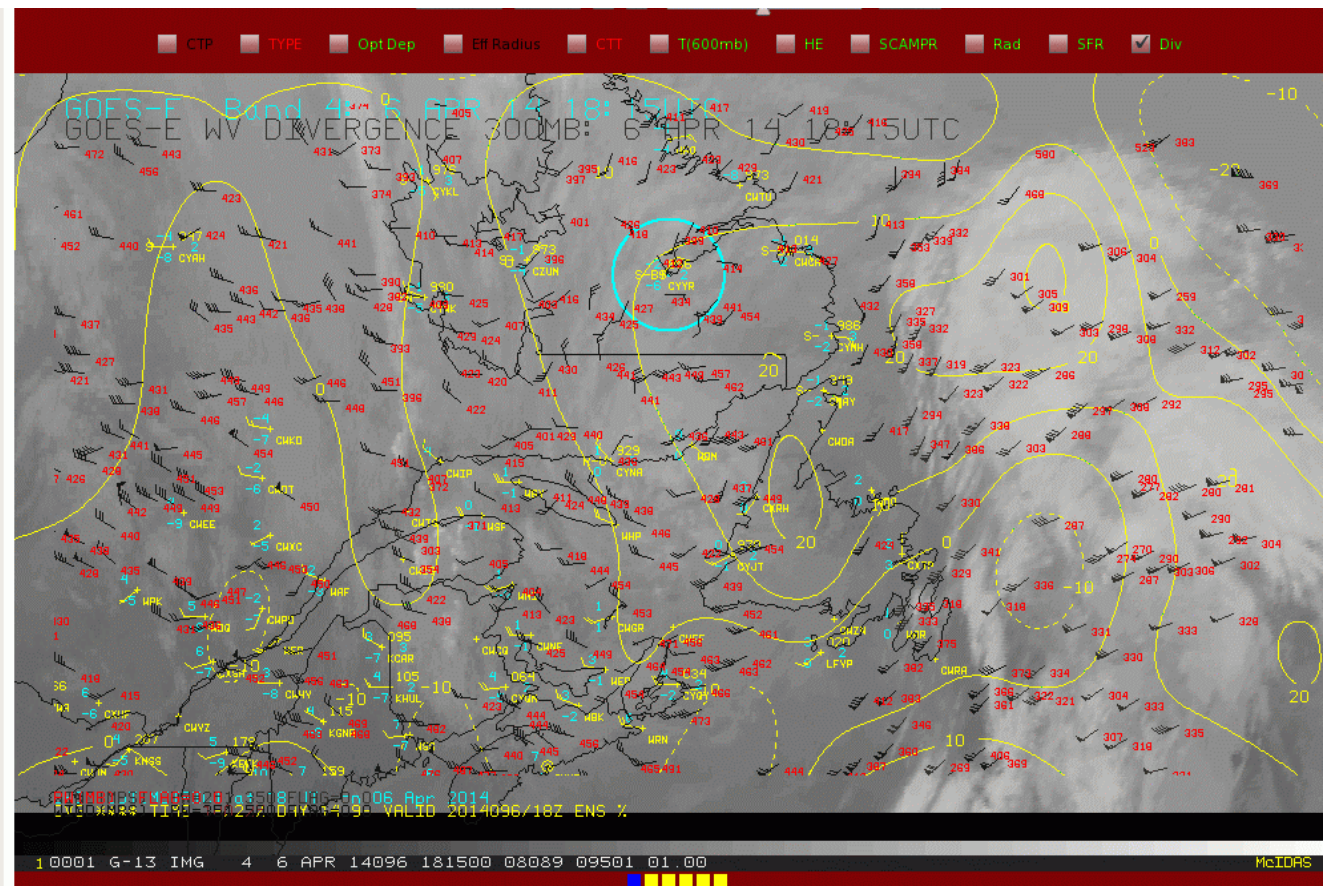
Figure 12c. Same as Fig. 12a except for 18:15 UTC.
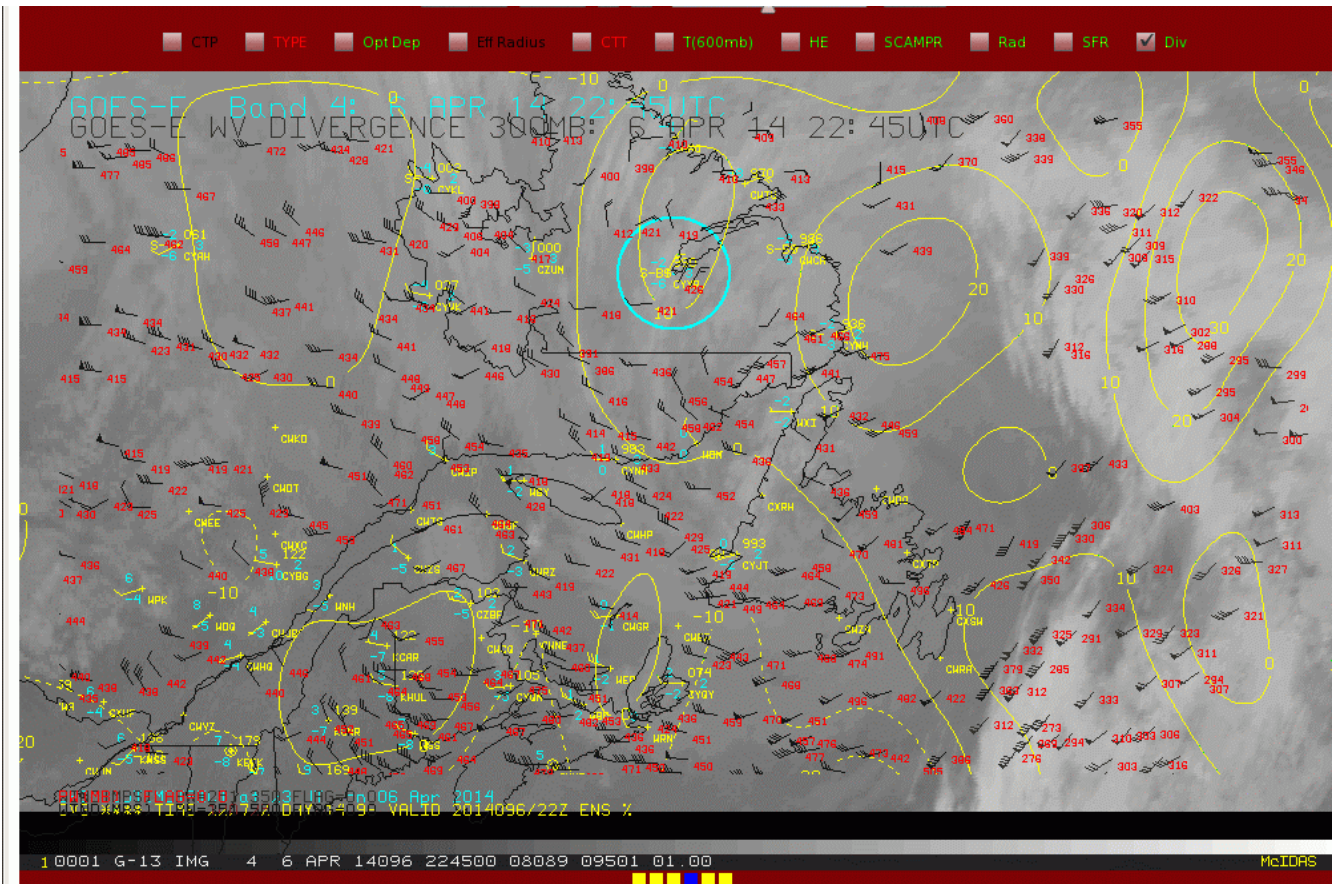
Figure 12d. Same as Fig. 12a except for 22:45 UTC.
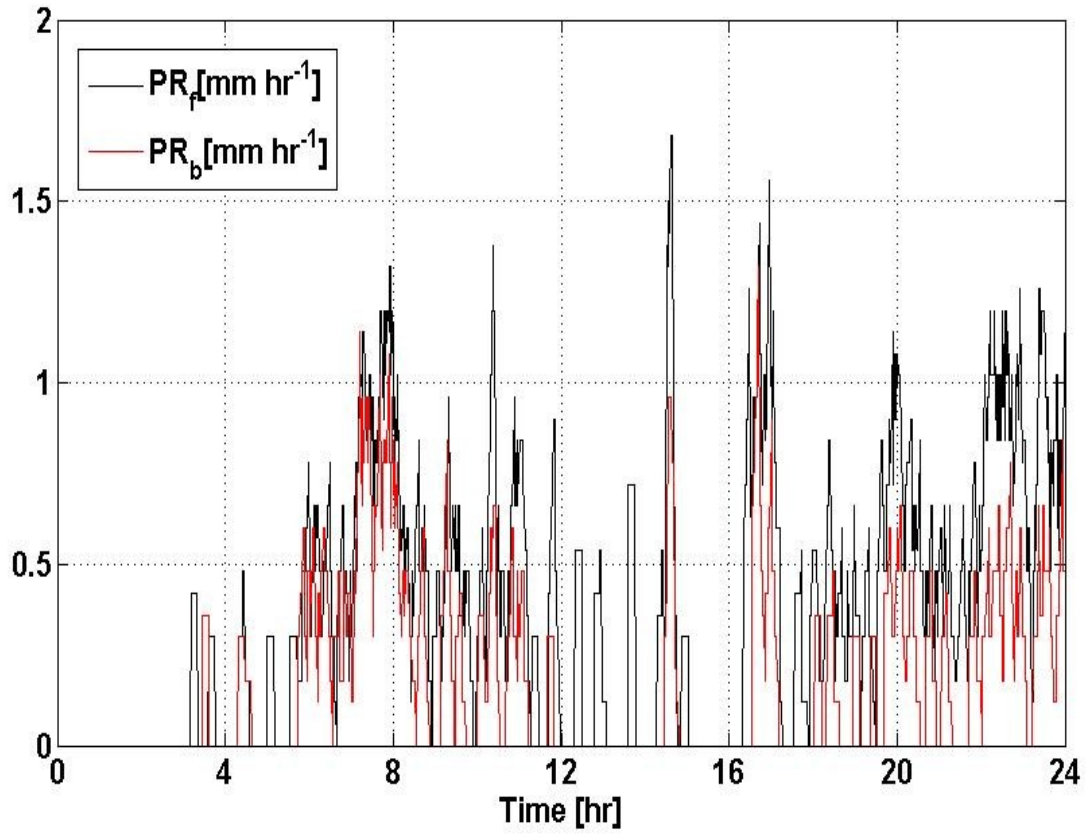
Figure 13. Precipitation rate (mm hr^{-1}) near Goose bay on 6 April 2014. Station "f" and "b". Times are UTC.
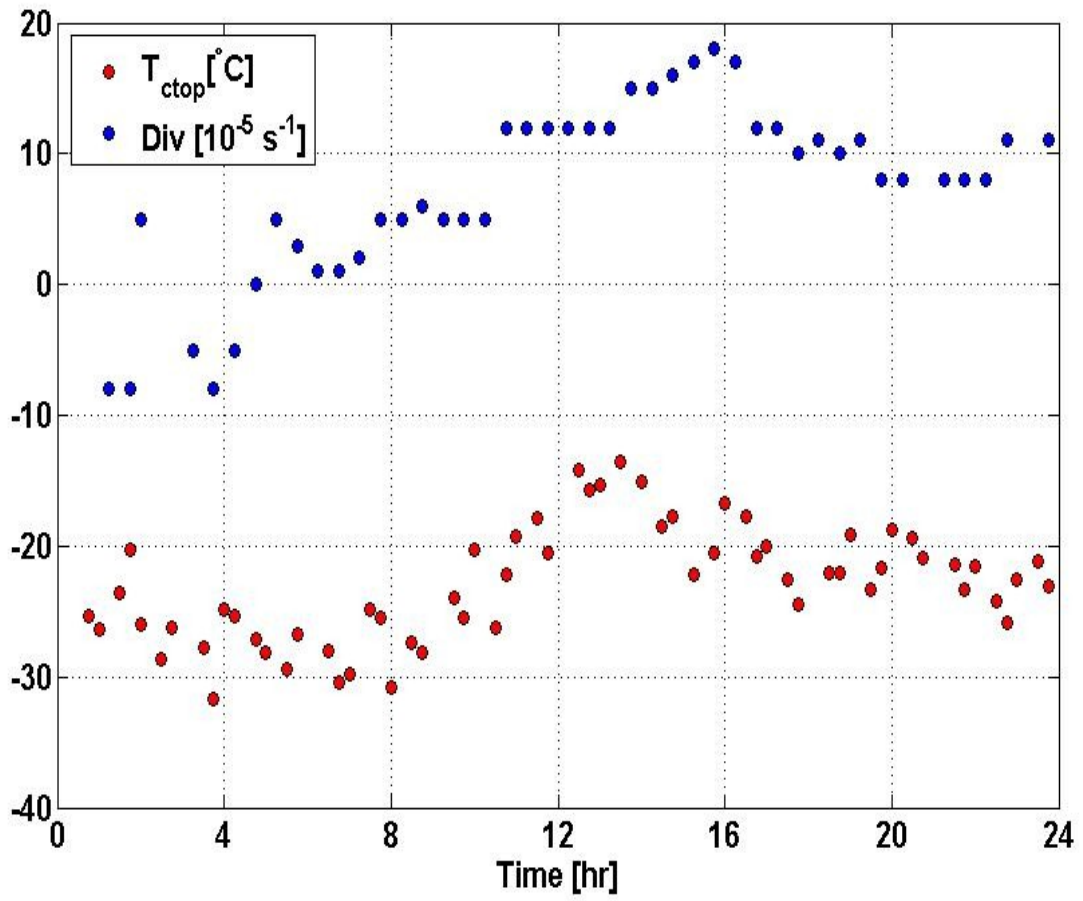
Figure 14. Divergence at 300 hPa (10^{s-1}) and cloud top temperature on 6 April 2014.
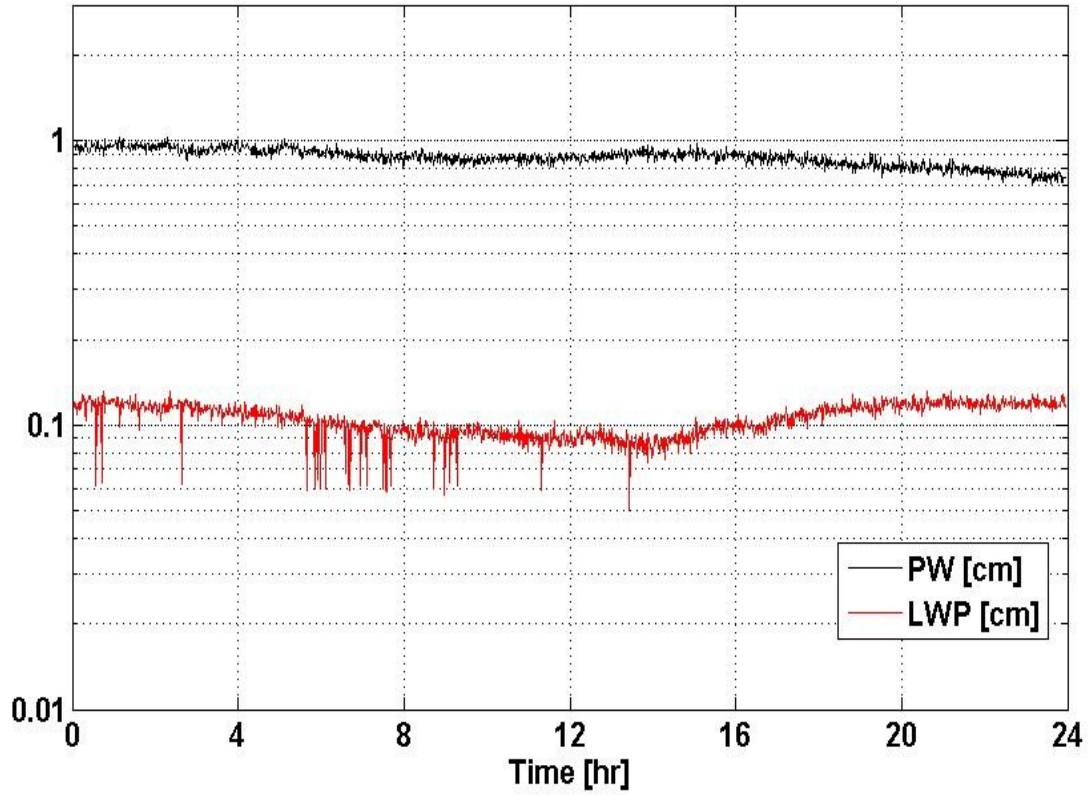
Figure 15. Integrated Precipitable Water (PW) and Liquid Water Path (LWP) on 6 April 2014. Times are UTC.
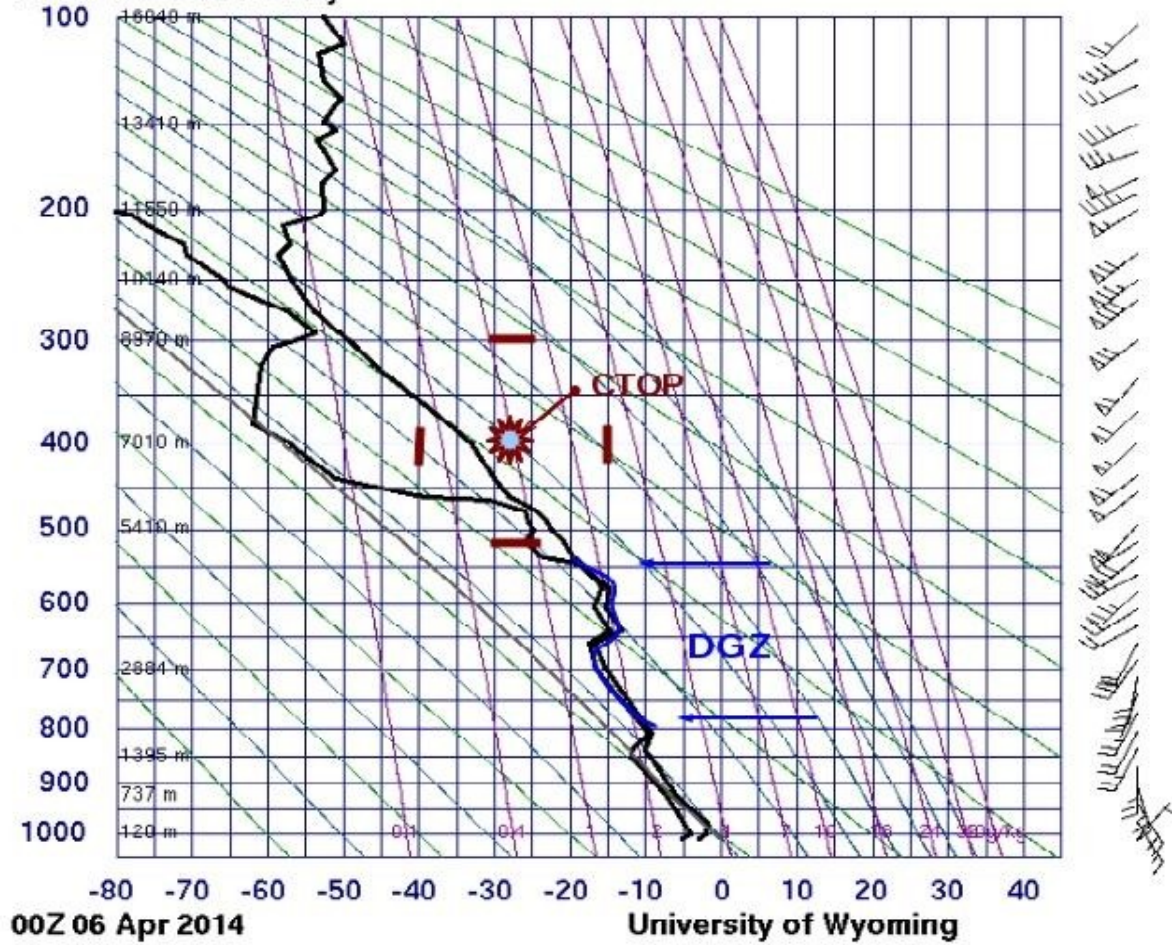
Figure 16a. Observed rawinsonde plot 06 April 2014 00 UTC near Goose Bay. Estimated cloud top from GOES (CTOP) with uncertainties in temperature and pressure. Top of dendritic ice growth zone from GOES (DGZ).
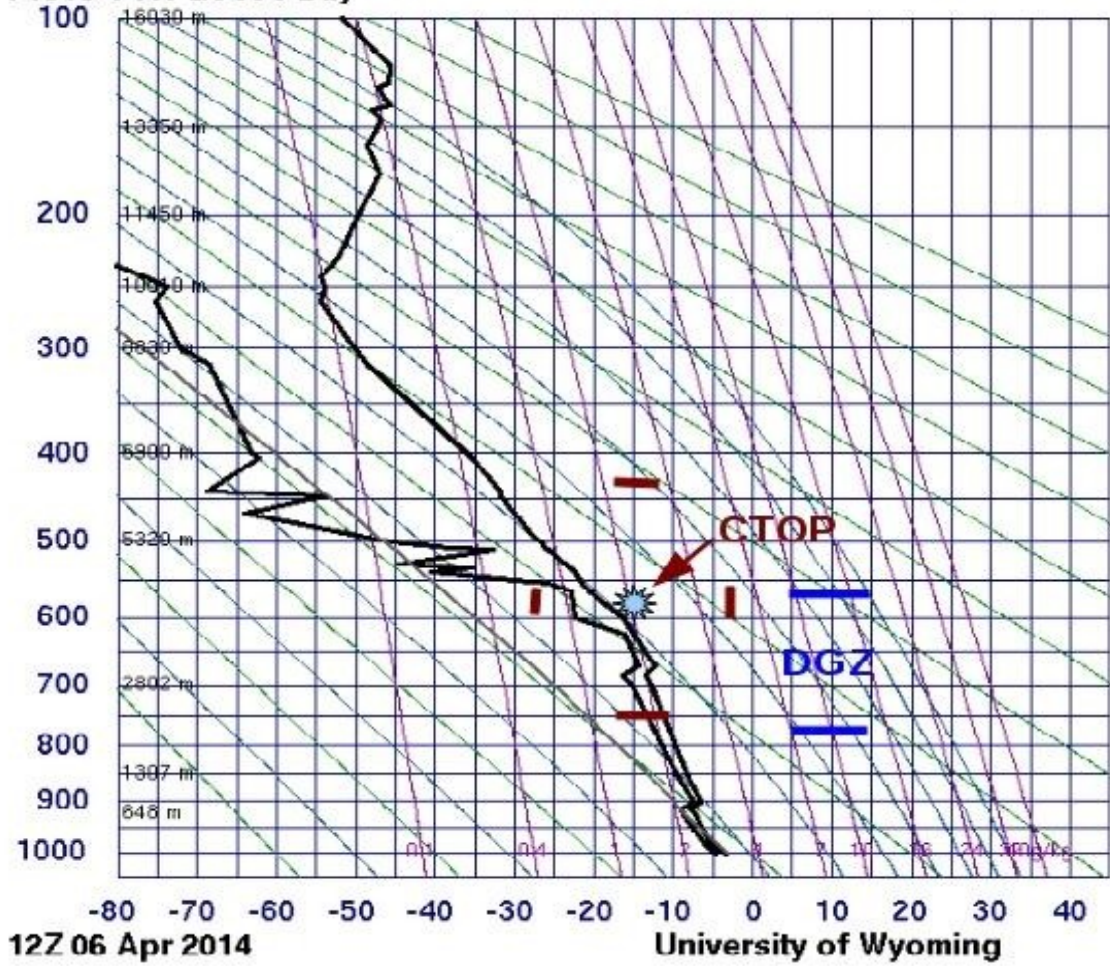
Figure 16b. Same as Fig. 16a except for 06 April 12 UTC.
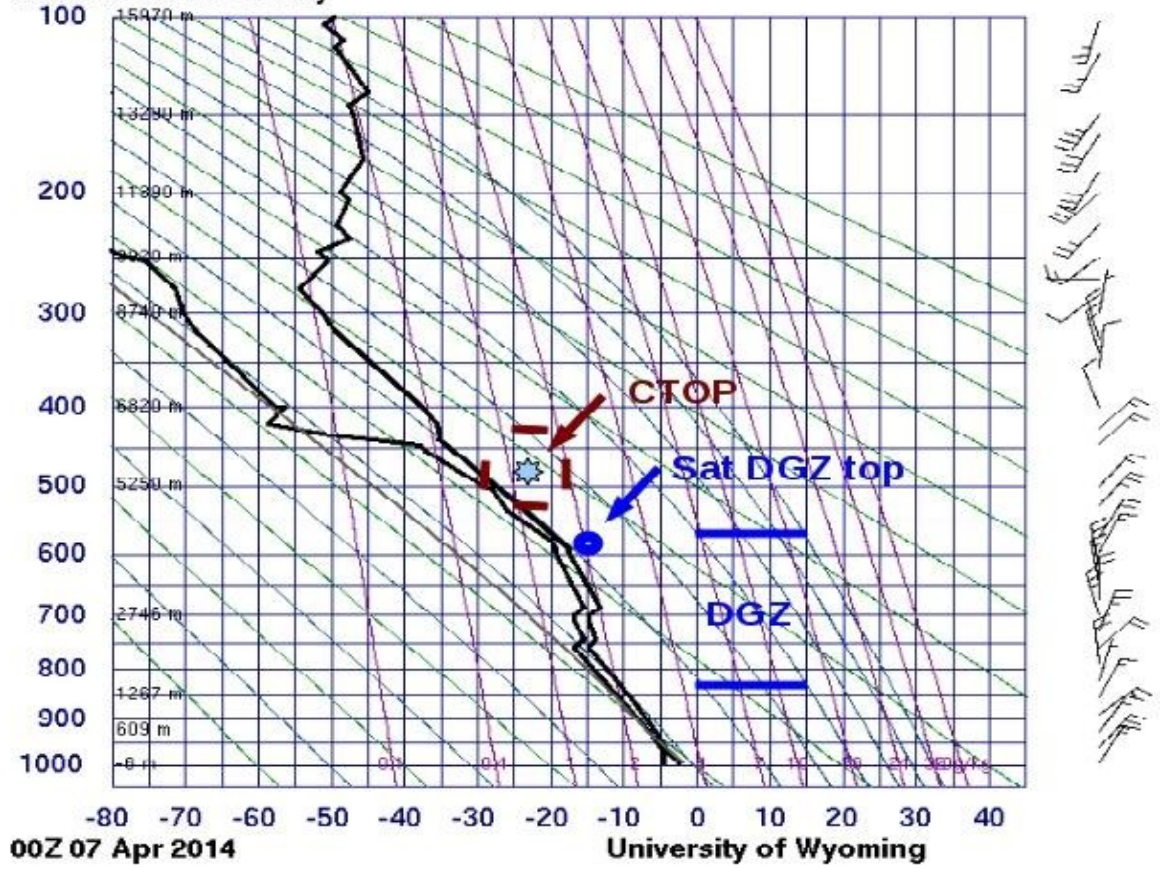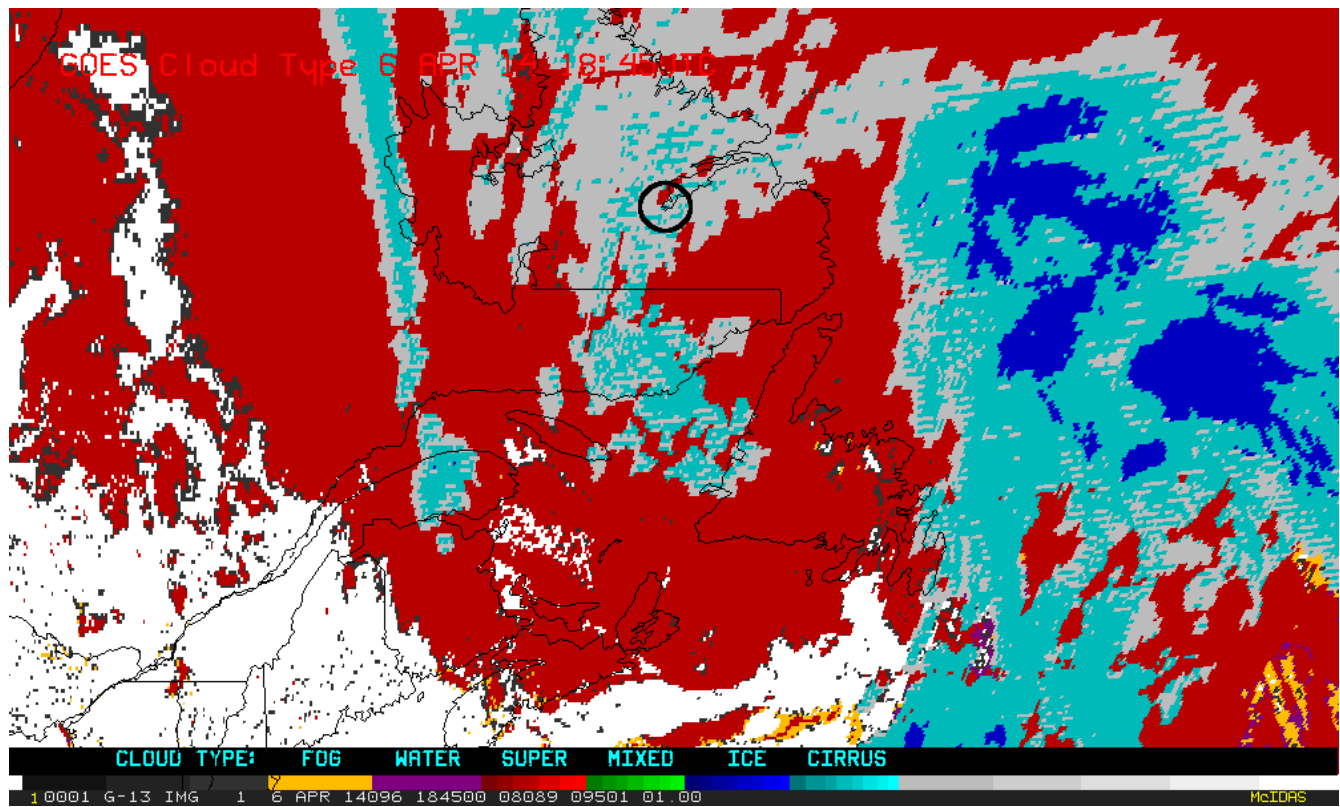
Figure 16c. Same as Fig. 16a except for 07 April 00 UTC.

Figure 17. Cloud type retrieved from GOES data at 1845 UTC 6 April 2014. Approximate location of ground-based sensors near Goose Bay, NL is indicated by the circle.
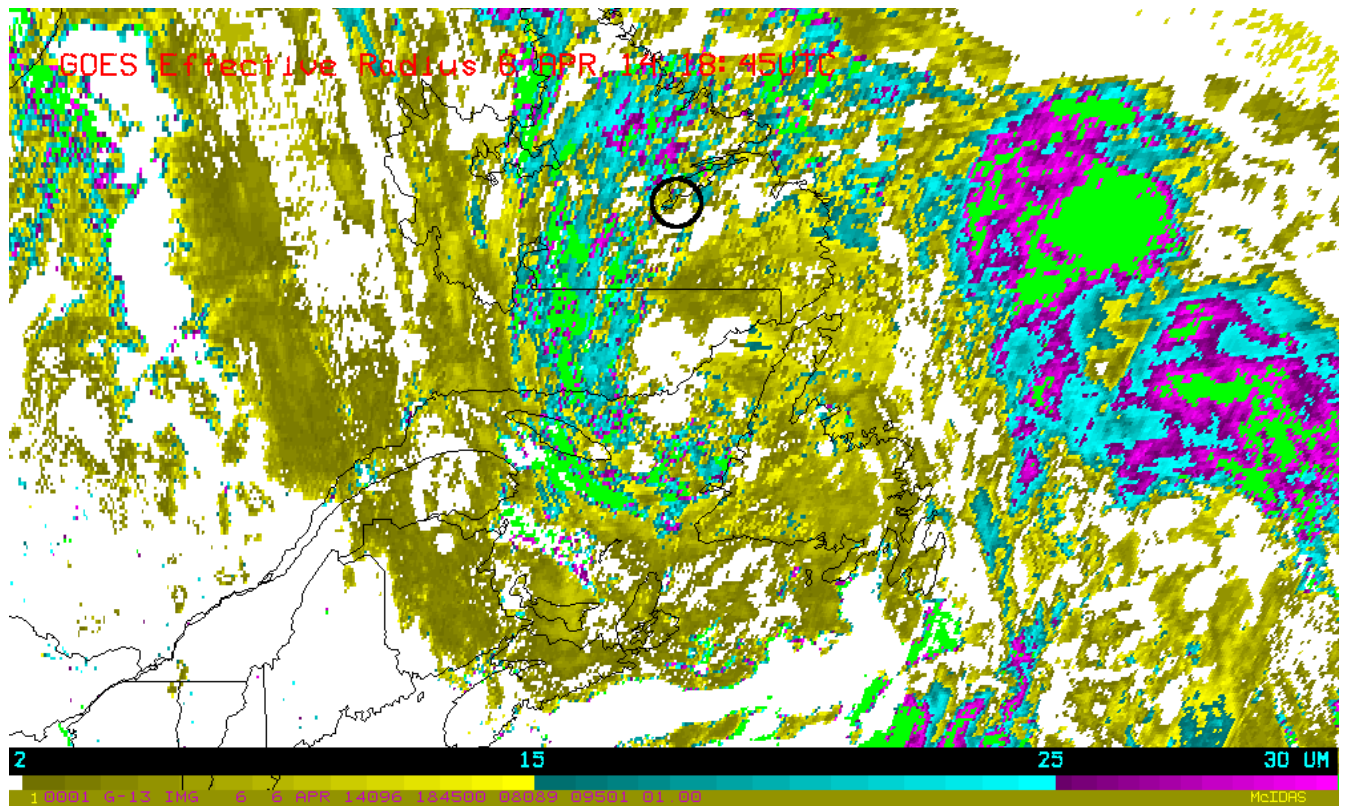
Figure 18. Effective cloud top particle radius (in microns) retrieved from GOES data at 1845 UTC 6 April 2014.
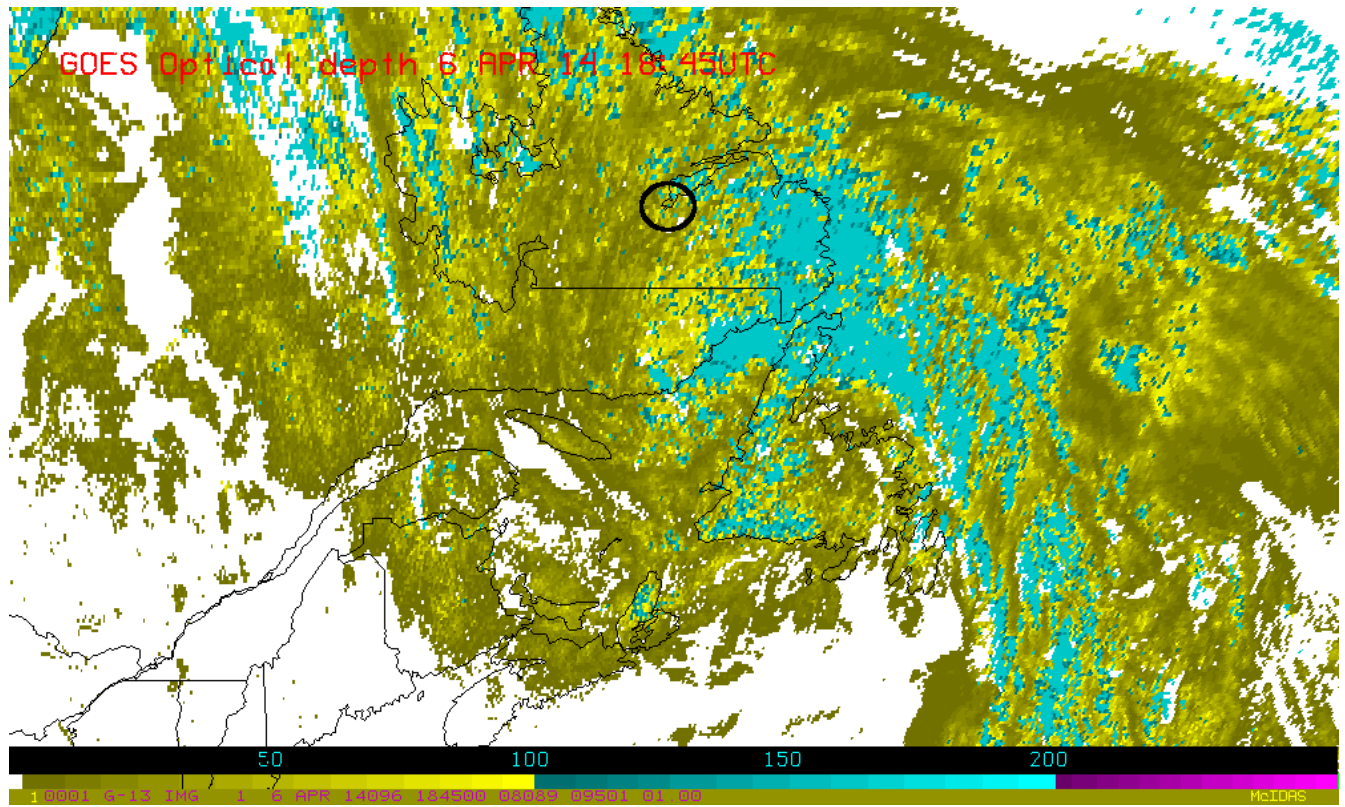
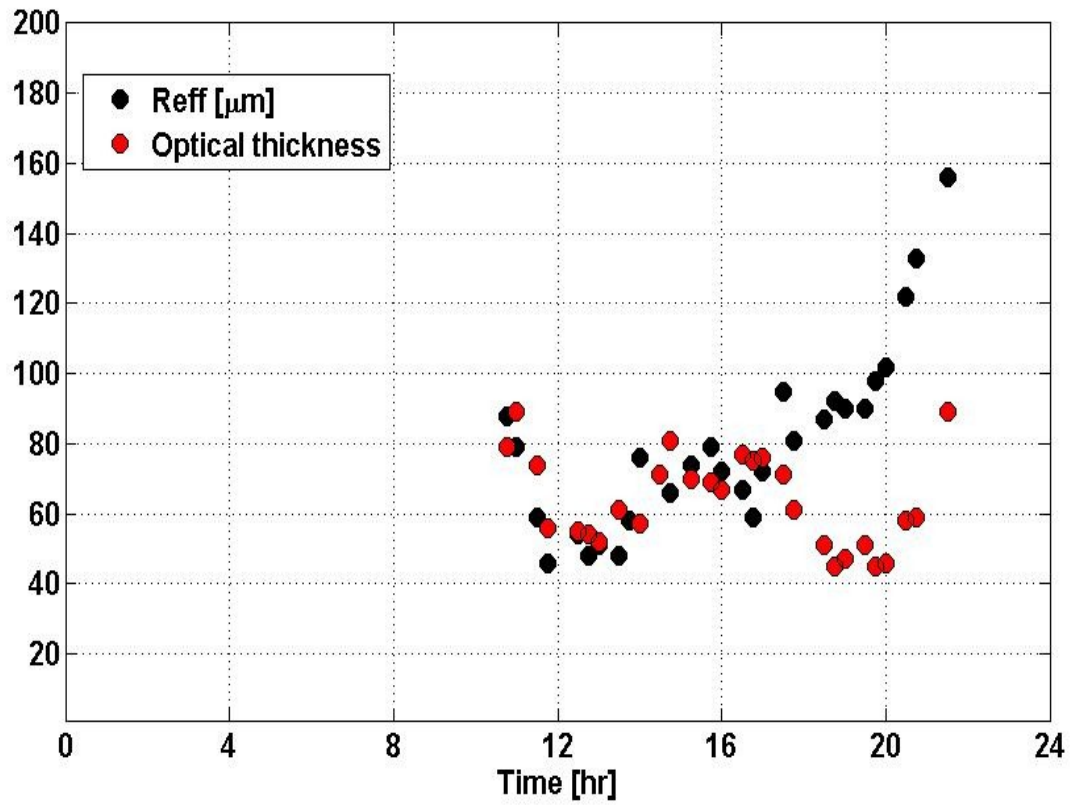Figure 19. Cloud optical depth retrieved from GOES data at 1845 UTC 6 April 2014.

Figure 20. Cloud top effective radius and optical depth on 6 April 2014. Times are UTC.